Sub-solar electron temperatures in the lower Martian ionosphere

W.K. Peterson[1], L. Andersson[1], R. Ergun[1], Ed Thiemann[1], Marcin Pilinski[1], S. Thaller[1], C. Fowler[2], D. Mitchell[2], M. Benna[3], R. Yelle[4], and Shane Stone[4].

[1]LASP, University Colorado Boulder
[2]Space Science Laboratory, University of California, Berkeley
[3]NASA Goddard Space Flight Center, Greenbelt, Md.
[4]University of Arizona

Submitted to JGR Space Physics November, 2019

Abstract:

Martian sub-solar electron temperatures obtained below 250 km are examined using data obtained by instruments on the Mars Atmosphere Evolution Mission (MAVEN) during the three sub-solar deep dip campaigns and a one-dimensional fluid model. This analysis was done because of the uncertainty in MAVEN low electron temperature observations at low altitudes and the fact that the Level 2 temperatures reported from the MAVEN Langmuir Probe and Waves (LPW) instrument are more than 400 Kelvin above the neutral temperatures at the lowest altitudes sampled (~120 km). These electron temperatures are well above those expected before MAVEN was launched. We find that an empirical normalization parameter, neutral pressure divided by local electron heating rate, organized the electron temperature data and identified a similar altitude (~160 km) and time scale (~2,000 s) for all three deep dips. We show that MAVEN data are not consistent with a plasma characterized by electrons in thermal equilibrium with the neutral population at 100 km. Because of the lack data below 120 km and the uncertainties of the data and the cross sections used in the one dimensional fluid model above 120 km, we cannot use MAVEN observations to prove that the electron

temperature converges to the neutral temperature below 100 km. However, the lack of our understanding the electron temperature altitude profile below 120 km does not impact our understanding of the role of electron temperature in determining ion escape rates because ion escape is determined by electron temperatures above 180 km.

Introduction:

The Mars Atmospheric Volatile EvolutioN (MAVEN, Jakosky et al., 2015) mission objective is to obtain reliable observations of geophysical parameters that control or limit atmospheric escape. Several processes such as the escape of energetic oxygen atoms depend strongly on the plasma electron temperature (e.g. e.g. Fox and Hac, 2009; Andersson et al., 2010; Lillis et al. 2015; Ergun et al., 2016; Brecht et al., 2017). There have been many recent papers reporting analysis of electron temperatures and their effect on the Martian thermosphere (e.g. Ergun et al., 2015, 2016; Fowler et al., 2015; Mendillo et al., 2017; Flynn et al., 2017; Lillis et al., 2017; Thiemann et al., 2018; Xu et al., 2018; and Peterson et al., 2018). These reports have focused primarily on data acquired during normal operations, not during the nine so called deep dip intervals, where the MAVEN periapsis was maintained below 140 km for several days.

Electron temperature data from the first sub-solar deep dip campaign have been analyzed by Ergun et al., (2015) and Peterson et al., (2018). They reported Electron temperatures at 130 km less than 500 Kelvin but greater than the observed neutral temperature of ~100 Kelvin (Stone et al., 2018). The 500 Kelvin value for electron temperature reported at 130 km is significantly larger than was expected before MAVEN was launched (e.g. Fox, 1993, Shinagawa and Cravens, 1989; Bougher et al., 2015; and Brecht et al., 2017).

Ergun et al., (2015), and others have noted that the MAVEN electron temperatures reported in the level 2 data product are known to biased high at low temperatures (i.e. T_E < 700 Kelvin). The measurement uncertainties reported in the level 2 data product are empirically derived as described in Fowler (2016). These empirical uncertainties are conservative estimates that are quite large being on the order of ±300 Kelvin for a 500 Kelvin electron temperature.

The purpose of this paper is to use MAVEN data acquired during the three MAVEN sub-solar deep dip intervals and analysis to improve our understanding of the electron temperature altitude profiles below 160 km.

Observations

The MAVEN spacecraft performed nine deep dip campaigns, three of which sampled the sub-solar region. During a deep dip campaign, the Martian thermosphere is sampled at altitudes below 140 km for periods on the order of a week. The latitudes and longitudes sampled in deep dip campaigns DD2, DD8, and DD9 in the Mars-centered Solar Orbital (MSO) coordinate system are shown in Figure 1. DD2 (deep dip 2) was from April 17 to 22, 2015; DD8 was from October 16 to 23, 2017; and DD9 was from April 24 to 30, 2018. Solar irradiance in three selected wavelength bands from the MAVEN Extreme UltraViolet Monitor (EUVM, Epavier et al., 2015 is presented in Figure 2. It shows that DD2 occurred early in the mission when solar activity was higher than during DD8 and DD9.

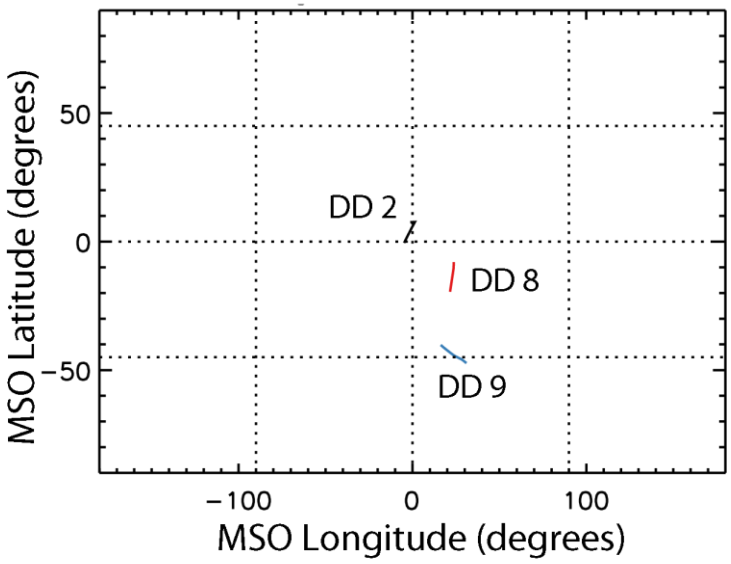

Figure 1: Location in MSO latitude and longitude of the periapsis location of the inbound segments of MAVEN orbits from the three sub-solar deep dip campaigns. DD2 (deep dip 2) was from April 17 to 22, 2015; DD8 was from October 16 to 23, 2017; DD9 was from April 24 to 30, 2018

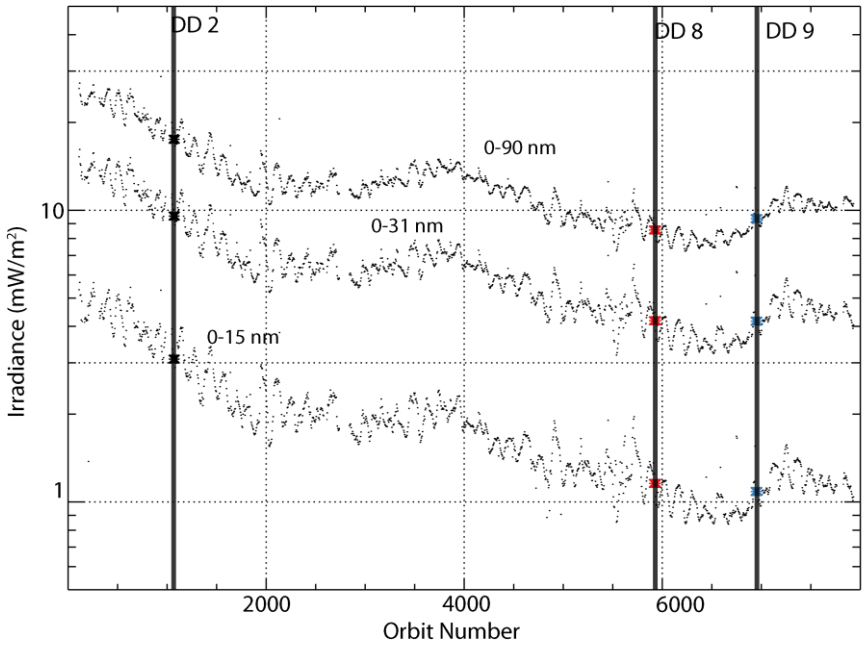

Figure 2. Solar EUV irradiance at Mars in the three indicated wavelength bands from the EUVM Level 3 daily spectral product. The orbit number range of the deep dip campaigns are indicated by the solid vertical lines.

Figure 3 presents the neutral, ion, and electron densities observed during the three deep dip campaigns from the MAVEN Neutral Gas and Ion Mass Spectrometer (NGIMS, Mahaffy et al., 2015) and Langmuir Probe and Waves (LPW, Andersson et al., 2015) instruments. Electron and neutral data are presented for each orbit in the in the left column and as the median of all observations in the right column. Median thermal Ion densities for the deep dip campaigns from the NGIMS instrument are also shown in the right column. To eliminate effects of crustal magnetic fields in their analysis, Peterson et al., (2018) considered only photoelectron data from orbits where the magnetic field (Connerney et al., 2015) was nearly horizontal to the Martian surface, i.e. for magnetic dip angles less than 30°. In Figure 3 electron and neutral densities obtained for magnetic dip angles less than 30° are indicated by red lines and black for dip angles larger than 30°. Below 200 km the divergence between the red and black electron density data is minimal, indicating that magnetic field orientation does not significantly affect ion and neutral densities. Careful examination of Figure 3 also shows that the sum of the O^+ and O_2^+ densities is less than the reported electron density (N_E) for all three deep dip campaigns. This difference is attributed to issues relating to the variable spacecraft potential, the limited energy range of the NGIMS instrument, and other instrumental effects. The magnitude of the difference in ion and electron density determinations is small compared to other uncertainties in the calculation of cooling terms in the heat equation as discussed in Peterson et al., (2018).

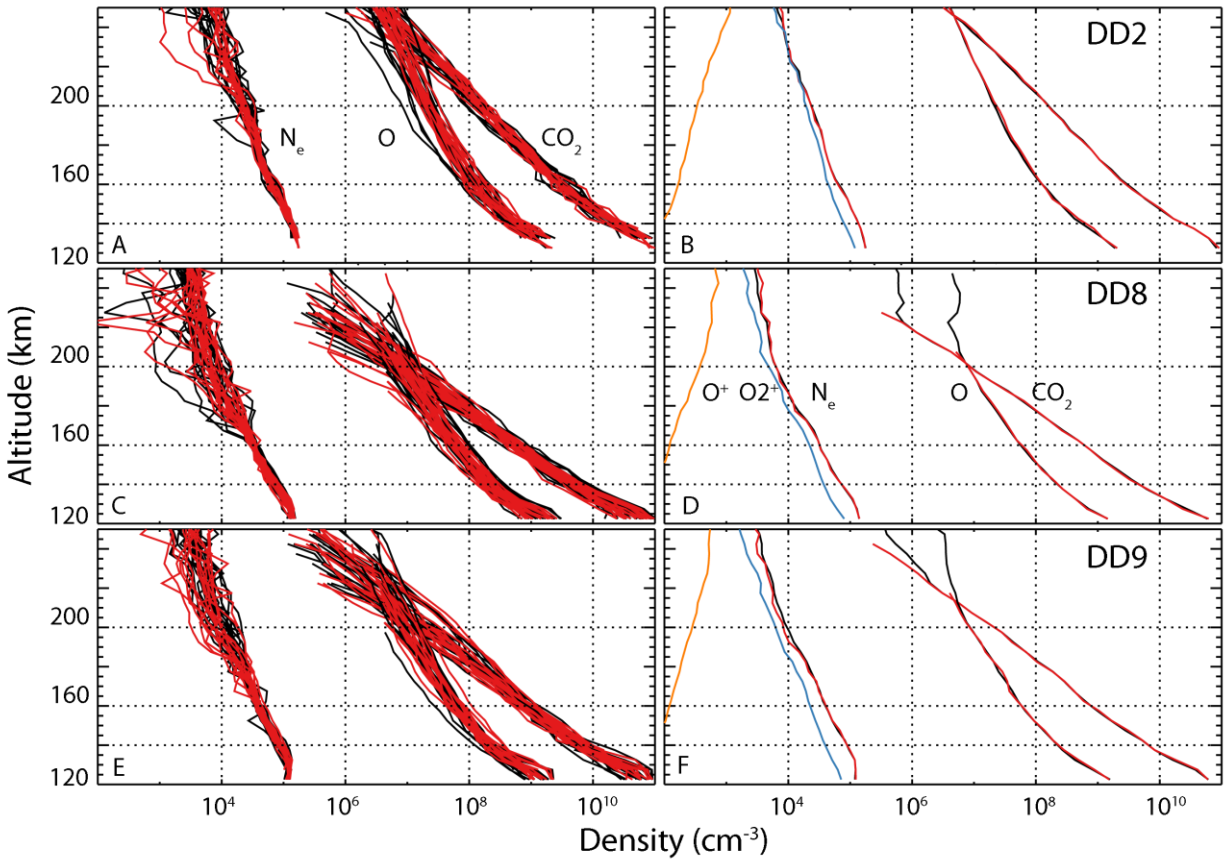

Figure 3: Electron, ion, and neutral densities from the three sub-solar deep dip campaigns for altitudes below 250 km. Panels A, C, and E show data for individual orbits; panels B, D, and F show the median values for all orbits in the deep dip campaign. In all panels electron, CO_2, and O densities are shown using both red and black colors. Red indicates orbits where the magnetic dip angle is less than 30° and black for orbits where it is not. In panels B, D, and E median densities of O^+ and O_2^+ are indicated by orange and blue lines respectively.

Observed electron temperatures (T_E) below 250 km from the three sub-solar deep dip campaigns are shown for each orbit in panels A, C, and E of Figure 4 and their median values in panels B, D, and F. Red indicates that the magnetic dip angle was less than 30°; black indicates that the magnetic dip angle was larger than 30°. Shown also in panels B, D, and F are neutral temperatures (T_N blue) reported by Stone et al, (2018), empirically derived upper and lower limits of the electron temperature (dashed lines, Fowler, 2016) and low altitude empirically

111 adjusted electron temperatures (discussed below and shown by green and orange lines). The
112 Andersson electron spike feature, an expected increase in electron temperatures at low sub-
113 solar altitudes (Andersson et al., 2019) is seen in the median values (panels B, D, and F) near
114 152 km in DD2 and 132 km in DD8 and DD9. No systematic difference in the electron
115 temperature profile as a function of dip angle is seen below 250 km, consistent with the results
116 of Sakai et al. (2019) obtained from a much larger data sample. Measured ion temperatures
117 from the Supra Thermal and Thermal Ion Composition instrument (STATIC, McFadden et al.,
118 2015) are not reported in Figure 4 because algorithms to account for all instrumental effects
119 encountered at thermal energies are not yet available (J. McFadden, private communication,
120 2019).
121

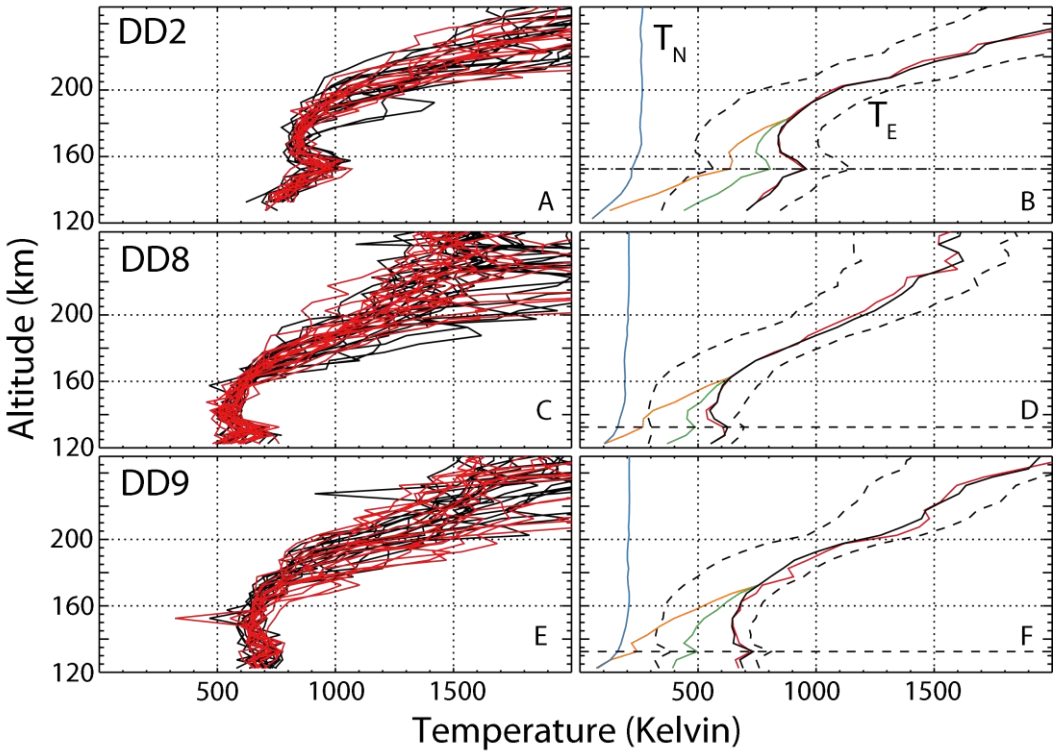

Figure 4: Electron temperatures from the level 2 data product obtained below 250 km from the three sub-solar deep dip campaigns are shown on a per orbit basis in panels A, C, and E. Their median values are shown in panels B, D, and F. As in Figure 3 red lines indicate data from orbits where the magnetic dip angle is less than 30° and black indicates where the dip angle is greater. Also shown in panels B, D, and F are neutral temperatures (blue) reported by Stone et al, (2018), empirically derived upper and lower limits of the electron temperature (dashed lines, Fowler et al., 2016) and low altitude empirically adjusted electron temperatures (green and orange lines, see text). The dashed horizontal lines in panels B, D, and F indicate the altitude of the Andersson T_E spike.

Below ~700 Kelvin, MAVEN electron temperatures reported in the level 2 LPW data product are known to be biased high (Ergun et al., 2015; Fowler, 2016, Peterson et al., 2018). The theoretical lower limit of the measurement is between 150 and 200 Kelvin. The upward bias in the value reported in the level 2 data likely arises from non-ideal behavior with regards to the operation of the Langmuir Probe in the highly variable plasma environment at Mars, including: variable sheath shape and size, ion wakes behind the probes, and non-uniform probe surfaces due to atomic oxygen contamination of the probe surfaces (Fowler 2016). The fitting process described in Fowler (2016) attempts to account for these non-ideal behaviors.

However, because LPW instrument is the first Langmuir Probe to be flown in such a variable plasma environment, there are no other comparable Langmuir Probe data sets with which to make comparisons and fully quantify these effects. The lower and upper temperature limits reported for the L2 data are subsequently quite conservative (Fowler, 2016). A re-examination of the fitting procedures used to obtain level 2 electron temperatures concluded that the values reported below 700 Kelvin are at most biased 25% too high (Ergun, private communication 2019). The empirically derived upper and lower limits of the electron temperatures are shown as dashed lines in Figure 3. These conservative limits are more than 25% above and below the reported values.

A concept, rationale, and procedure to empirically adjust raw electron temperatures below 160 km obtained by the LPW instrument were presented in Peterson et al., (2018). Extrapolations are made from altitudes and temperatures where, prior to the MAVEN launch, it was generally assumed that electrons and neutrals were in thermal equilibrium at ~100 Kelvin between 80 and 120 km (e.g. Gröller, Montmessin, Yelle, et al., 2018) to altitudes and temperatures where the uncertainties in T_E observed by the LPW instrument are low compared to the observed values. Two extrapolations of T_E are shown in Figure 4 panels B, D, and F for all three deep dips. Orange lines show temperatures derived assuming electron-neutral thermal equilibrium at 100 Kelvin at 120 km. Green lines show temperatures derived assuming electron-neutral thermal equilibrium at 100 Kelvin at 80 km. The extrapolations retain the Andersson T_E spike feature (Andersson et al., 2019).

Electron temperature is determined by a balance between heating and cooling rates of electrons, ions, and neutrals. On the dayside, the primary source of energy for heating

electrons is the photoelectron population. Figure 5 presents the median photoelectron spectrum obtained from the MAVEN Solar Wind Electron Analyzer (SWEA) instrument (Mitchell et al., 2016) as a function of energy at altitudes indicated by the color code from each of the three dip campaigns. Photoelectron data are not obtained below 3 eV. The photoelectron data have been corrected for spacecraft potential and averaged over 5 km wide altitude bins. Data are shown centered at altitudes of 122 km (black), 127 km (red), 152 km (blue), and 182 km (green).

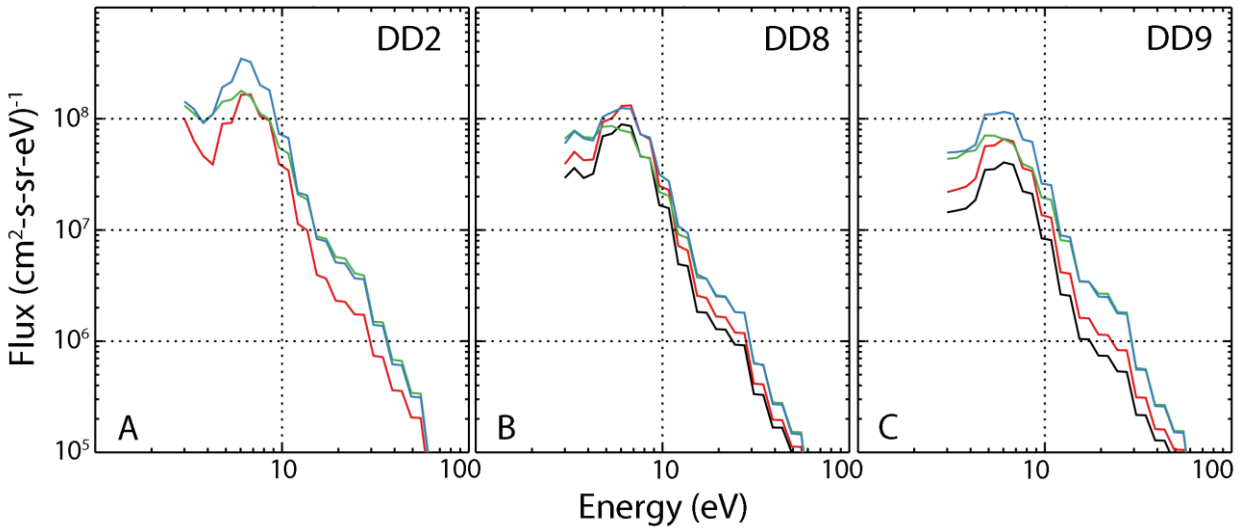

Figure 5: Median photoelectron fluxes as a function of energy from the three indicated sub-solar deep dip campaigns. The 5 km wide altitude bins over which the data are averaged are indicated by black (122 km), red (127 km), blue (152 km), and green (182 km). Note that during deep dip 2 (DD2), data were not obtained below 125 km.

Figure 6 presents the low energy portion of the photoelectron distributions seen in Figure 5 and thermal electron fluxes calculated from a Boltzmann distribution using the observed electron density and temperatures shown in Figure 4 as a function of energy for the lowest altitude bin sampled during each of the three sub-solar deep dips. The solid black line above 3 eV is a reproduction of photoelectron fluxes reported in Figure 5 at 127 km (DD2) and 122 km

(DD8 and DD9). The Boltzmann distributions shown were calculated from the lowest altitude electron densities shown in Figure 3 and the five electron temperature values at the lowest altitude sampled for the observed (level 2 data) in solid black lines, the upper and lower limits reported in the level 2 data (dashed black lines), the extrapolation to 120 km (orange lines), and the extrapolation to 80 km (green lines).

Dalgarno, McElroy, and Moffett (1963), and Rees (1989) have formulated empirical relations to calculate local thermal electron heating rates from photoelectron energy spectra. Both of these approaches involve an integral of the photoelectron flux above the energy, E_{CO}, where the thermal energy flux is equal to the photoelectron energy flux. As seen in Figure 6, and confirmed by calculations not illustrated here, E_{CO} is below 3 eV in all cases. In particular, the major contribution to the Rees and Dalgarno et al. integrals occurs for energies below 3 eV. Thus, the photoelectron flux observations above 3 eV shown in Figures 5 and 6 do not directly determine electron heating rates; the secondary electrons they produce both locally and deeper in the atmosphere do. Peterson et al., (2018) developed an alternative method to calculate the local electron heating rates which is used and discussed below.

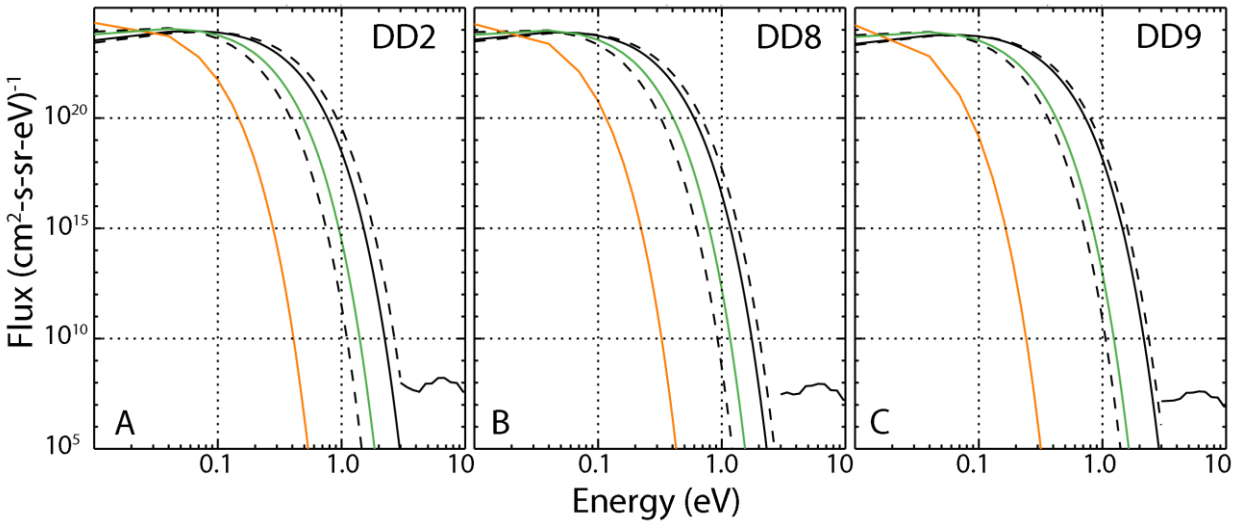

Figure 6: Thermal and photo electron energy spectra for the three deep dip campaigns at the lowest observed altitude. The solid black lines above 3 eV are reproduced from the lowest altitude photoelectron energy spectrum in Figure 5. The solid black line below 3 eV is a Boltzmann distribution calculated using the lowest altitude T_E and N_E values reported in the LPW level 2 data product. The dashed black lines are calculated using the upper and lower limits of T_E and N_E in the level 2 data product. The solid green and orange lines are calculated using the empirically adjusted temperatures shown in Figure 4.

Analysis and Discussion:

An alternative statement of the objective of this paper is to determine which, if any, of the five low altitude temperature extrapolations shown in Figure 4 are consistent with both other MAVEN observations and our current understanding of electron thermalization processes. Because there are no observations of the thermal/photoelectron energy spectrum near E_{CO}, we must rely on a fully kinetic model of the thermal and photoelectron plasma, or the fluid model developed over 40 years ago and described by, among many others, Schunk and Nagy (2009), Mata et al., (2014), and Peterson et al., (2018). Here we use the one-dimensional fluid model and cross sections presented by Mata et al., (2014) and Peterson et al., (2018). The method does not use a photoelectron transport code. It uses the concept of electron heating efficiency

to account for the transfer of energy produced by photoionization to local electrons. Local thermal electron heating and cooling rates for each of the electron temperature profiles are calculated as described below.

Figure 7 presents EUV energy deposition and electron heating rate profiles for the three sub-solar deep dip campaigns. The black line with + symbols in Figure 7 shows energy deposition associated with photoionization calculated from the neutral densities shown in Figure 3 and a Solar EUV spectrum constrained by MAVEN observations (Thiemann et al., 2017). The other lines in Figure 7 show the sum of thermal electron cooling rates, convection, advection, and expansion rates calculated using MAVEN data shown in Figures 3 and 4 and the five low altitude temperature extrapolations shown in Figure 4. Note that these calculations and those by Peterson et al., (2018) use the Campbell et al, (2008) inelastic e-CO_2 cross section instead of the Dalgarno (1969) cross sections given as equation A12 by Matta et al., (2014). This approach includes electron – ion and electron – neutral collisions and approximates the ion temperature (T_I) as the average of T_E and T_N.

Assuming thermal equilibrium, the electron heating rate equals the sum of the cooling, convection, advection, and expansion rates (e.g. Mata et al., 2004, Peterson et al., 2018). Above ~ 160 km electron energy deposition is greater than the local electron heating rates. This arises because energetic photoelectrons produced above 160 km transport significant energy to lower altitudes.

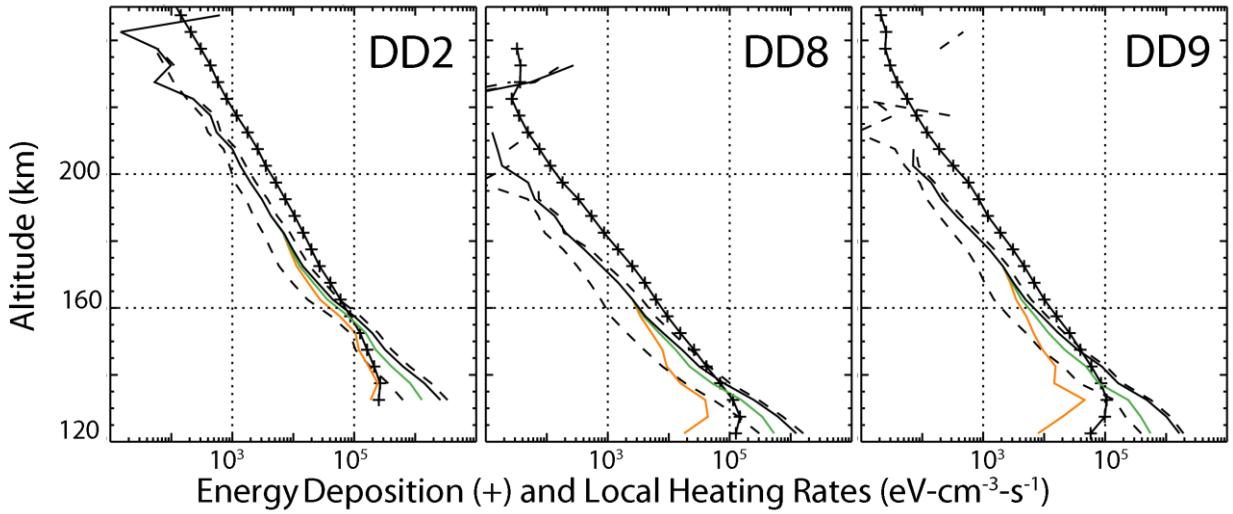

Figure 7: Energy Deposition (black lines with + symbols) and the sum of cooling, advection, conduction, expansion, conduction and local electron heating rates calculated using the one-dimensional model described by Mata et al., (2014) and Peterson et al., (2018). Sums are shown for the 5 temperature altitude profiles shown in Figure 4. The solid black line was calculated using the T_E and N_E values in the LPW level 2 data product. The dashed black lines are calculated using the upper and lower limits of T_E and N_E in the level 2 data product. The solid green and orange lines are calculated using the empirically adjusted temperatures shown in Figure 4. Note that under the assumption of local thermal equilibrium the sum of the cooling, advection, conduction, expansion, conduction terms is equal to the local thermal electron heating rate.

Peterson et al., (2018) defined electron heating efficiency as ratio of the local electron heating rates to the energy deposition rate. This approach does not require a photoelectron transport code or the calculation of ionization efficiencies (e.g. Cui et al., 2018). Figure 8 shows the inferred electron heating efficiency as a function of altitude for the three deep dip campaigns and the five low altitude temperature extrapolations under consideration. Electron heating efficiencies above 100% indicate that energetic photoelectrons produced at higher altitudes are transporting and depositing their energy at lower altitudes. Above ~200 km, heating efficiencies are not well organized by altitude and are sometimes negative, especially for deep dips 8 and 9. Above ~200 km the heat conduction term in the heat equation becomes significant and variable (Peterson et al., 2018). Other contributions to the variability above ~200

km come from temporal and spatial variations in the inputs to the heat equation not captured in the deep dip average values used in the calculations of cooling, advection, conduction, and expansion, rates. See, for example, Fowler et al., (2018a, b). Figure 8 demonstrates that electron heating efficiency below ~200 km depends strongly on the electron temperature.

Four of the five electron heating efficiency altitude profiles exceed 100% between 130 and 160 km; one of them (the temperature extrapolation to 100 Kelvin at 120 km, indicated by orange lines) does not. Errors in the calculating the heating efficiency are large because the calculation involves the sum of many terms as described in Peterson et al., (2018). A similar error analysis shows that the reported heating efficiencies greater and less than 100% in Figure 8 are statistically significant.

An altitude profile of heating efficiency that does not exceed 100% above the altitude of peak EUV absorption (~ 120 km) is not physically realistic because it implies that there is no region in the Martian ionosphere where transport of energetic photoelectrons from higher altitudes is significant. We conclude that the electron temperature profile extrapolated to 100 Kelvin at 120 km is not consistent with MAVEN data and the one-dimensional model we used.

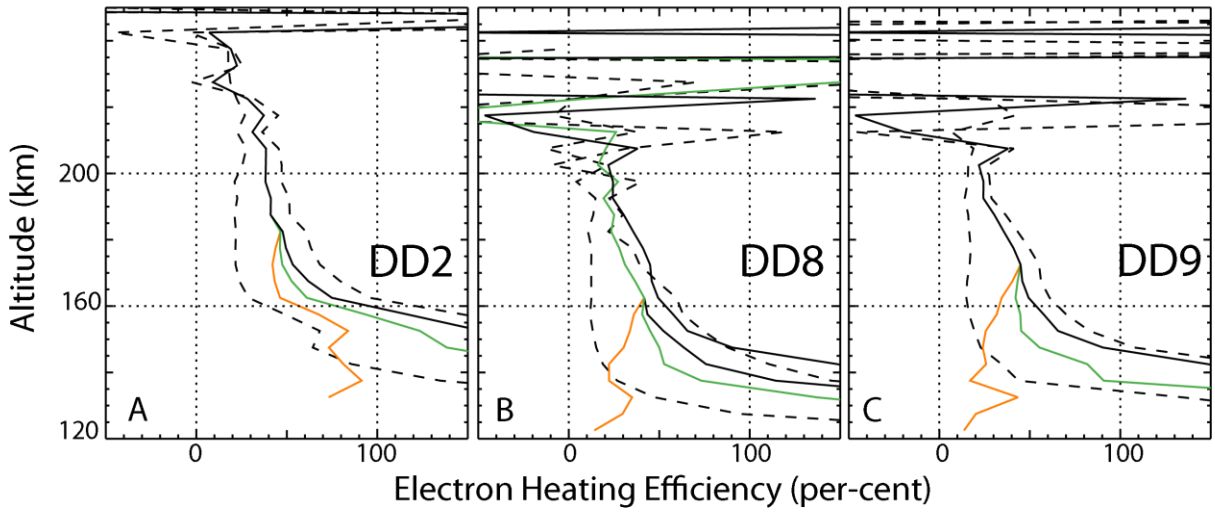

Figure 8: Inferred electron heating efficiencies as a function of altitude for the three deep dip campaigns and the five low altitude temperature extrapolations under consideration. The solid black line was calculated using the T_E and N_E values in the LPW level 2 data product. The dashed black lines are calculated using the upper and lower limits of T_E and N_E in the level 2 data product. The solid green and orange lines are calculated using the empirically adjusted temperatures shown in Figure 4. The profile using the lowest temperatures indicated by solid orange lines was found to be non-physical (see text).

Electron temperature altitude profiles vary systematically with EUV irradiance and Martian season. Data exploration not illustrated here demonstrated that plotting T_E as a function of neutral pressure divided by the local electron heating rate (P/LEH) reduced some of the systematic variability with season and EUV irradiance. Here neutral pressure is the product of neutral density (CO_2 and O from Figure 3) and neutral temperature (Figure 4). Local electron heating is calculated as the product of EUV energy deposition (Figure 7) and electron heating efficiency (Figure 8). We note that the units of P/LEH are seconds.

Figure 9 presents P/LEH as a function of altitude for each of the sub-solar deep dip campaigns calculated using four electron temperature profiles: The LPW Level 2 values (solid black lines) and empirical upper and lower limits (dotted black lines) as well as the empirical

290 temperature profile that reaches 100 K at 80 km (solid green lines). For DD2 MAVEN data were
291 not acquired at the lowest altitudes and therefor the heating rate calculations are not available.
292 The systematic errors in calculating heating efficiency discussed above preclude using the P/LEH
293 parameter above ~200 km in the sub-solar region. Shown also in Figure 9 are the altitudes of
294 the Andersson T_E spike (vertical dashed lines), and the altitudes where the optical depth of EUV
295 irradiance is 1 and 3 (vertical dashed dotted lines). Optical depth 1 and 3 correspond to
296 altitudes where 63% and 95% of the incident EUV irradiance is absorbed respectively. Optical
297 depth of 3 occurs near 160 km for all cases, but optical depth of 1 varies over a wide altitude
298 range in the three deep dip campaigns investigated.
299 The shape of the P/LEH vs. altitude plots has two regions of different slope separated by a
300 knee located near the altitude where the optical depth is approximately three. Below this
301 altitude energetic photoelectron production is less important. The knee occurs for P/LEH values
302 between 1000 and 2000 seconds or a frequency of ~10^{-3} seconds. These times / frequencies are
303 not characteristic of any of the local plasma parameters, being an order of magnitude larger
304 than the typical O_2^+ ion gyro period. This time scale is more characteristic of planetary scale
305 thermospheric motions.

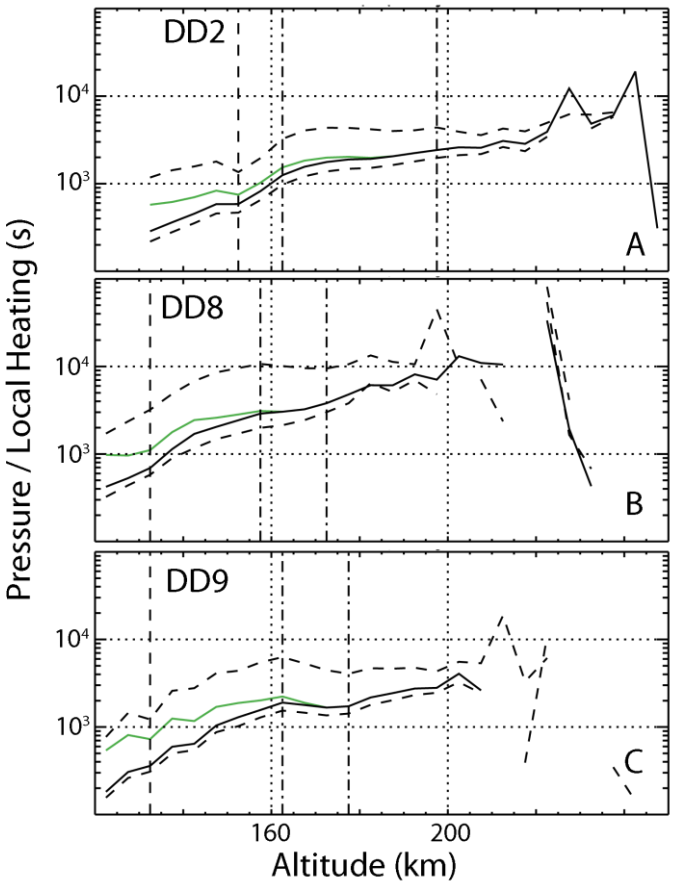

Figure 9. Altitude vs neutral pressure over local heating rates (P/LEH). Data are shown for 4 T_E profiles. Solid black present the LPW Level 2 values. The black dashed lines present the empirical upper and lower limits from the LPW Level 2 data product. The green lines present empirical TE extrapolations to 100 Kelvin at 80 km. The altitudes of the Andersson T_E spikes are shown by vertical dashed lines. The altitudes where the optical depth of EUV irradiance is 1 and 3 are shown by vertical dashed dotted lines. See text.

Figure 10 presents Electron temperature as a function of altitude (left, panels A, C and E) and electron temperature as a function of the ratio of neutral pressure to local electron heating rate (P/LEH) right, panels B, D, and F). The color code and line styles follows those in Figure 9. In panels A, C, E dashed vertical lines are shown at the altitude of the observed Andersson T_E spike. The dash dot vertical lines in panels A, C, and E are shown where the EUV optical depth is 1 and 3. The data in panels B, D, and F show that the variations in T_E as a function of season and

solar cycle follow more similar patterns when compared to the altitude distributions seen in panels A, C, and E.

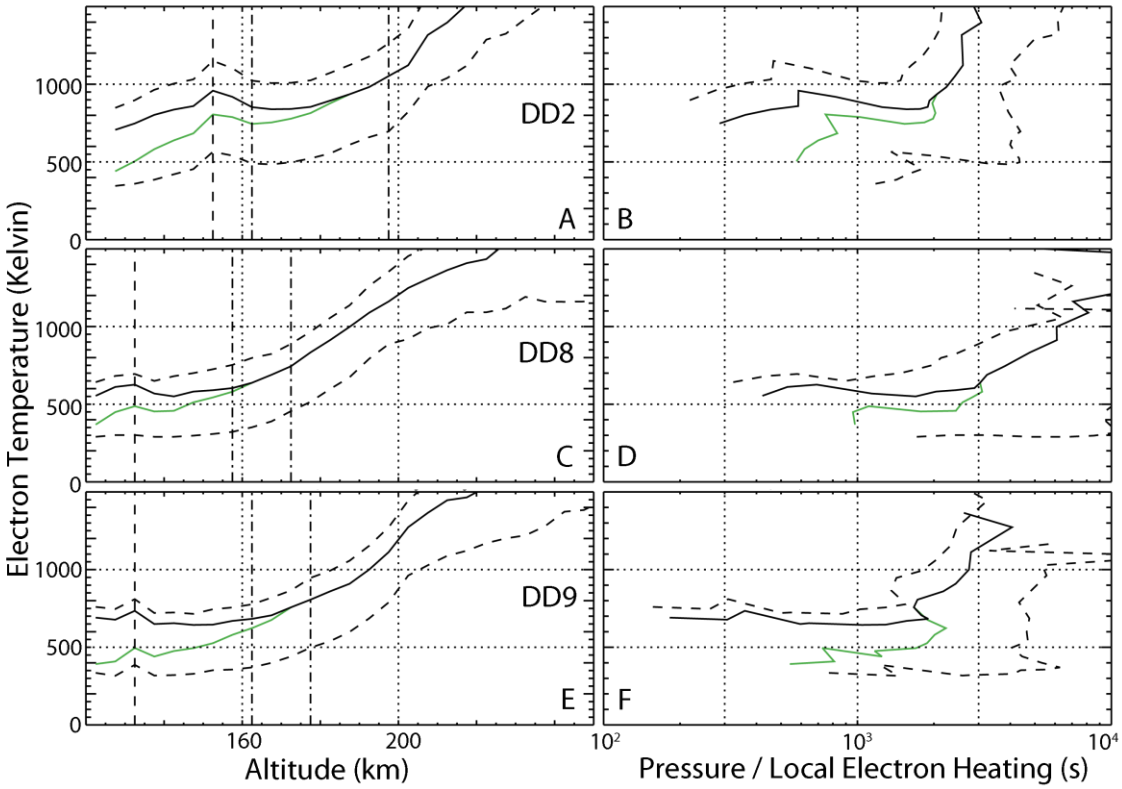

Figure 10: Electron temperature as a function of altitude (left, panels A, C and E) and electron temperature as a function of the ratio of neutral pressure to local electron heating rate (P/LEH, right, panels B, D, and F). The color code and line styles follows that in Figure 9. Values calculated using the reported LPW level 2 electron temperature values are shown as solid black lines. Values calculated using the empirical upper and lower electron temperature values are shown as dashed black lines. Values calculated using the extrapolation to 100 Kelvin at 80 km are shown as green lines. In panels A, C, E dashed vertical lines are shown at the altitude of the observed Andersson T_E spike. The dash dot vertical lines in panels A, C, and E are shown where the EUV optical depth is 1 and 3 i.e. 63% and 95% of the incident solar EUV irradiances has been absorbed above this altitude. See text.

The four different temperature altitude profiles in panels A, C, and E of Figure 10 differ in slope. The reported Level 2 temperature profiles and their empirical upper and lower limits (solid and dashed black lines) have a smaller slope below the altitude where the optical depth is about 3. The data in panels B, D, and F show that T_E data are essentially independent of the

P/LEH parameter below 2-3 x 10^3 seconds. Above 2-3 x 10^3 seconds the T_E vs. P/LEH data have approximately constant slopes with different values of the slope for each deep dip. The knee in the P/LEH vs. altitude plot in Figure 9 near the altitude with an optical depth of three is located below 2-3 x 10^3 s in the T_E vs. P/LEH display.

The data presented in panels B, C, and F raise two questions that are related to the relative importance of electron thermalization processes as a function of altitude. 1) What is the significance, if any, of T_E being relatively independent of P/LEH below ~2-3 x 10^3 seconds? 2) What is the significance, if any, of the value 2-3 x 10^3 seconds?

The answer to question 2 is uncertain. 2-3 x 10^3 seconds and its associated frequency are not characteristic of any local plasma parameters but rather are characteristic of planetary scale thermospheric motions. It is difficult to interpret this answer in terms of Martian thermospheric properties however. Since ion and/or neutral motion on this time scale is associated with planetary scale thermospheric motions, it is not clear how this time scale comes from our calculations using in-situ observations and a one-dimensional (vertical) model with the assumptions of local thermal equilibrium. Transport of energy associated with ions and neutrals is not considered in our formulation. Transport of electron energy is included in our calculations only as a function of altitude.

Regarding question 1: What is implied by the fact that T_E is independent of a parameter, such as pressure divided by local heating (P/LEH) below ~ 200 km and above the 120 km lower limit of our observations (and for values of P/LEH below 2-3 x 10^3 s)? The answer is ambiguous. It is commonly assumed that electrons equilibrate to the neutral temperature at some low altitude. The observed neutral temperatures shown in Figure 4 are well below the

approximately constant electron temperature for P/LEH at values less than 2-3 x 10^3 seconds for all four temperature profiles considered in Figure 10. These facts imply either that T_E falls to the value of T_N (~ 100 Kelvin) well below 120 km (200 seconds in units P/LEH) or our one-dimensional code which uses some poorly determined cross sections and an empirical ion temperature profile does not adequately account for energy transfer between and among ions, neutrals, and electrons at the low temperatures encountered at low altitudes on Mars.

Finally, we compare the electron temperature profiles discussed above with recent predictions and/or models of Martian electron temperatures at altitudes below 160 km in Figure 11. As in Figures 9 and 10, solid black lines indicate the observed temperature reported in the MAVEN/LPW level 2 archived data product. The dashed black lines are the empirical upper and lower temperatures as described by Fowler (2018a) and reported in the level 2 data product. The solid purple line is drawn at 75% of the level 2 T_E. As noted above, a re-analysis of selected data lead to the conclusion that the level 2 T_E upward bias is less than 25%. Below ~ 200 km the uncertainty in the reported T_E is significantly less the empirical estimate reported in the level 2 data product and indicated by dashed black lines. The solid green line presents the empirical low altitude temperature extrapolation to 100 Kelvin at 80 km presented in Figure 4. Recent temperature profiles from Ergun et al., (2015, dashed green lines), Withers et al., (2014, dashed orange lines), and Sakai et al., (2016, dashed blue lines) are also shown in Figure 11. The Ergun et al., (2015) fit to the deep dip 2 data is consistent within the empirical observational uncertainties of all of MAVEN/LPW temperatures for all altitudes in all three deep dip intervals. The electron temperatures profiles reported Sakai et al., (2016) extended to 100 km and were calculated for orbits before deep dip 2 and are therefore most comparable to the data obtained

384 in deep dip 2. The Sakai electron temperature calculations are consistently below those
385 reported above from all other sources at all altitudes.
386 The electron temperatures derived following the analysis of Withers et al., (2014, dashed
387 orange lines in Figure 11) used the observational solar zenith angles, and three parameters, T_N,
388 Zpp and Ho. The dashed orange curves with the highest temperature at 80 km uses Zpp=120
389 km, Ho 10 km and a neutral temperature (T_N) of 100 Kelvin. The dashed orange curve with the
390 lowest temperature at 80 km uses Zpp=100 km, Ho=10km and a neutral temperature of 75
391 Kelvin. Both temperature profiles derived using the Withers' relations are consistently below
392 MAVEN / LPW values above about 150 km. The Withers et al., analysis suggests a stronger
393 dependence of electron temperature with altitude above ~ 120 km than those reported in the
394 LPW level 2 data products (black solid and dashed lines), Sakai et al., (2016, blue dashed lines),
395 and the empirical extrapolation to 100 Kelvin at 80 km (solid green lines).
396

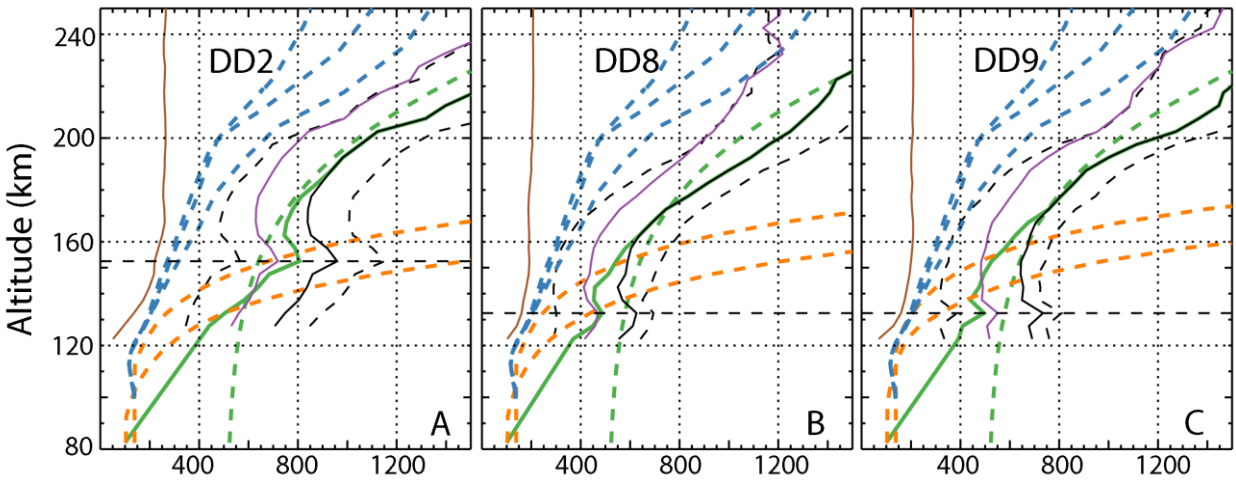

Figure 11. Electron temperature comparisons for the three sub-solar deep intervals. Solid black lines are the MAVEN/LPW T_E data from the level 2 data product. Black dashed lines present the empirical upper and lower limits of MAVEN/LPW T_E given in the level 2 data product. The solid purple line is 75% of the level 2 electron temperature (see text). The solid green line is the empirical low altitude/temperature extrapolation to 100 Kelvin at 80 km reproduced from Figure 4. The solid brown line are neutral temperatures (Stone et al., 2018) reproduced from Figure 4. The dashed blue lines are from Sakai et al., (2016). The dashed green lines reproduce the best fit reported by Ergun et al., (2015). The dashed orange lines were calculated using relations reported by Withers et al., (2014) and the parameters noted in the text. Dashed horizontal lines are presented at the altitude of the Andersson T_E spike.

Below ~ 120 km the 4 temperature profiles shown in Figure 11 fall into two classes. The Ergun et al., (2015, dashed green lines) fit to deep dip 2 data that does not converge to the neutral temperature at lowest altitudes and all others. The other profiles all converge to a neutral temperature which is not measured but is an input to the calculation determining the profile. The Sakai et al., (2016, blue dashed lines) and Withers et al. (2014, orange dashed lines) fits are derived from approximations to the standard fluid model described by Schunk and Nagy (2009), with the neutral temperature used as an input parameter to calculating electron temperature. The empirical fit to the low altitude data indicated by the solid green line (Peterson et al., 2018) assumes an altitude and temperature where electrons and ions equilibrate. We note that the low altitude ~100 Kelvin neutral temperature observed by Stone

et al., (2018), and used by Sakai, Withers, and Peterson is at the low end of the neutral dayside temperatures reported from MAVEN EUVM observations by Gröller et al., (2018). The low altitude limit of electron temperature from the Ergun fit is well above the upper end of neutral dayside temperatures reported by Gröller et al., (2018).

Conclusions:

Electron temperatures and their empirical upper and lower limits reported in the MAVEN/LPW Level 2 data products from the three sub-solar deep dip campaigns of the MAVEN mission have been examined. The analysis was based on a one-dimensional formulation of the fluid model commonly known as the heat equation using data obtained from MAVEN instruments following the procedures described here and by Peterson et al., (2018). The method does not use a photoelectron transport code. It uses the concept of electron heating efficiency to account for the transfer of energy produced by photoionization at all altitudes to local electron heating. This approach requires knowledge of the local ion temperature, T_I. In this analysis T_I is assumed to be the average of T_E and T_N.

The electron temperature altitude profiles are consistent with previous results reported from the MAVEN/LPW instrument during normal, i.e. non deep dip operations (e.g. Fowler et al., 2018a, 2018b, and Peterson et al. 2018). The electron temperatures below ~200 km were also shown to be independent of magnetic field orientation, consistent with the results of Sakai et al., (2019)

The MAVEN/LPW electron temperatures reported in L2 data products are thought to be biased high. The difference between the empirical upper and lower limits originally reported in

442 the level 2 data product, are quite large (300 to 500 Kelvin) as shown in Figure 11. The re-
443 analysis of MAVEN/LPW data summarized above for electron temperatures less than 750 Kelvin
444 suggests that the upward bias in the Level 2 values is, at most, 25%, which is considerably
445 smaller than the empirical upper and lower limits of electron temperature included in the Level
446 2 data product.

447 The focus of the analysis presented above is on altitudes below 160 km. This analysis is
448 necessary because of the uncertainty in low electron temperature observations at low altitudes
449 and the fact that the Level 2 temperatures reported are more than 400 Kelvin above the neutral
450 temperatures at the lowest altitudes sampled (~120 km) which are well above those expected
451 before MAVEN was launched (e.g. Fox, 1993, Shinagawa and Cravens, 1989; Bougher et al.,
452 2015; and Brecht et al., 2017).

453 Following Peterson et al., (2018) we introduced empirical electron temperature altitude
454 profiles for the three deep dip campaigns that: 1) Reached 100 Kelvin at 120 and 80 km
455 respectively; 2) Merged with the electron temperature in the Level 2 data product above ~160
456 km; and 3) Retained the Andersson T_E spike below 160 km (Andersson et al., 2019). We
457 demonstrated that the lowest temperature profile, the one that reaches 100 Kelvin at 120 km,
458 when input to the heat equation, leads to the un-physical result that there is no region in the
459 Martian ionosphere where transport of energetic photoelectrons from higher altitudes is
460 significant.

461 To be better able to compare temperature profiles consistent with the heat equation
462 obtained during different Martian seasons and solar activity we examined electron temperature
463 as a function of pressure over local heating rates (P/LEH) in Figures 9 and 10. We found that

this display identified two temperature regimes in the observed data shown in solid black lines: Those above and below values of P/LEH of 2000-3000 seconds. Above this value electron temperature linearly increased with values of P/LEH. Below 2000 to 3000 seconds the electron temperature profiles were relatively independent of the P/LEH parameter in the range investigated. This is a time scale associated with planetary scale thermospheric motions. We could not identify a correlation of this time scale with any specific process.

An examination of recent model and data analysis of electron temperature below the 120 km MAVEN observational limit identified two classes:

1) Where the electron temperature was forced to converge on a neutral temperature that was empirically selected, not predicted. These include two based on the heat equation (Withers et al., 2014, and Sakai et al., 2016) and the empirical fit (shown as green lines in Figure 11). The neutral temperatures used were all at the low end of the range of neutral temperatures reported by Gröller et al. (2018);

2) Those not forced to converge on a neutral temperature. The Ergun et al., (2015) fit to observed deep dip 2 electron temperatures was made independent of any assumption on the neutral temperature. The low altitude limit of electron temperature from the Ergun fit is well above the upper end of neutral dayside temperatures derived from MAVEN optical observations and reported by Gröller et al., (2018).

Above 120 km, the analysis shows that the Sakai et al. (2016) temperature profiles are too low and inconsistent with the heat equation when MAVEN observations are used as input parameters. The Withers et al., (2014) model of low altitude electron temperatures is derived from three ad-hoc parameters (height, scale height, and neutral temperature). We found that,

between 120 and 160 km, there is consistency between the Withers' temperature profile using carefully selected input parameters and MAVEN observations. Above ~160 km, the Withers' predictions are all too high. The empirical fit to the data that converges to a 100 Kelvin neutral temperature at 80 km introduced here is also consistent with MAVEN observations. The Ergun et al., (2015) fit to DD2 data is consistent MAVEN observations for all three deep dip intervals considered.

Because of the lack of low altitude data and the uncertainties of the data and one dimensional one electron temperature fluid model above 120 km, we ***cannot*** use MAVEN observations to prove that the electron temperature converges to the neutral temperature below 100 km. The common wisdom is that T_E converges to T_N at some altitude, now below 100 km. If T_E does not converge to T_N, then a possible reason is that our one-dimensional code which uses an empirical ion temperature profile and some poorly determined cross sections does not adequately account for energy transfer between ions, neutrals, and electrons at the low temperatures encountered at low altitudes on Mars. Perhaps a particle in cell code which does not use assumed electron and ion temperature profiles will be able to resolve this question.

The lack of our understanding the electron temperature altitude profile below 120 km, however, does not impact our understanding of the role of electron temperature in determining ion escape rates because ion escape is determined above ~180 km (Ergun et al., 2016; Brecht et al., 2017).

Acknowledgements:

We thank the many 100's of people who made the MAVEN project successful. This work was sponsored by NASA through the Mars Exploration Program. MAVEN data are available on NASA's Planetary Data System.

References:

Andersson, L., R. E. Ergun, and A. I. F. Stewart (2010), The combined atmospheric photochemistry and ion tracing code: Reproducing the Viking lander results and initial outflow results, Icarus, 206(1), 120–129.

Andersson, L., R. E. Ergun, G. T. Delory, A. Eriksson, J. Westfall, H. Reed, J. McCauly, D. Summers, and D. Meyers (2015), The Langmuir probe and waves (LPW) instrument for MAVEN, Space Sci. Rev., doi:10.1007/s11214-015-0194-3.

Andersson, L., C.M. Fowler, A Nagy, R. Yelle, T. Cravens, S. Bougher, A.G. Burns (2016), Unexpected Diurnal Variations in Electron Temperature in the Mars Ionosphere, 2016 AGU Fall Meeting Paper SA51C https://agu.confex.com/agu/fm16/meetingapp.cgi/Paper/170321

Bougher, S. W., Pawlowski, D., Bell, J. M., Nelli, S., McDunn, T., Murphy, J. R., Chizek, M., and Ridley, A. (2015), Mars Global Ionosphere-Thermosphere Model: Solar cycle, seasonal, and diurnal variations of the Mars upper atmosphere. *J. Geophys. Res. Planets*, 120, 311–342. doi: 10.1002/2014JE004715.

Brecht, S. H., Ledvina, S. A., and Jakosky, B. M. (2017), The role of the electron temperature onion loss from Mars, *J. Geophys. Res. Space Physics*, 122, 8375– 8390, doi:10.1002/2016JA023510.

Campbell, L., M. J. Brunger, and T. N. Rescigno (2008), Carbon dioxide electron cooling rates in the atmospheres of Mars and Venus, J. Geophys. Res., 113, E08008, doi:10.1029/2008JE003099.

Connerney, J. E. P., et al., The MAVEN magnetic field investigation. Space Sci. Rev. 10.1007/s11214-015-0169-4 (2015). doi: 10.1007/s11214-015-0169-4

Cui, J., X.-S. Wu, S.-S. Xu, et al. (2018), Ionization efficiency in the dayside Martian upper atmosphere, Ap. J. Lett., 857:L18, https://doi.org/10.3847/2041-8213/aabcc6

Dalgarno, A, M.B. McElroy, and R.J. Moffett (1963), Electron temperatures in the ionosphere, Planet. Space Sci., 11, 463-484, doi: 10.1016/0032-0633(63)90071-0

Delgarno, A., 1969. Inelastic collisions at low energies. Can. J. Chem. 47, 1723–1729.

Eparvier, F. G., P. C. Chamberlin, T. N. Woods, and E. M. B. Thiemann (2015), The solar extreme ultraviolet monitor for MAVEN, Space Sci. Rev., doi:10.1007/s11214-015-0195-2.

Ergun, R. E., M. W. Morooka, L. A. Andersson, C. M. Fowler, G. T. Delory, D. J. Andrews, A. I. Eriksson, T. McEnulty, and B. M. Jakosky (2015), Dayside electron temperature and density

profiles at Mars: First results from the MAVEN Langmuir probe and waves instrument, *Geophys. Res. Lett.,* 42, 8846–8853, doi:10.1002/ 2015GL065280.

Ergun, R. E., et al. (2016), Enhanced O_2^+ loss at Mars due to an ambipolar electric field from electron heating, *J. Geophys. Res. Space Physics*, 121, 4668– 4678, doi:10.1002/2016JA022349.

Flynn, C. L., Vogt, M. F., Withers, P., Andersson, L., England, S., & Liu, G. (2017). MAVEN observations of the effects of crustal magnetic fields on electron density and temperature in the Martian dayside ionosphere. *Geophysical Research: Letters*, 44, 10,812–10,821. https://doi.org/10.1002/2017GL075367

Fowler, C. M., Andersson, L., Ergun, R. E., Morooka, M., Delory, G., Andrews, D. J., Lillis, R. J., McEnulty, T., Weber, T. D., Chamandy, T. M., et al. (2015), The first in situ electron temperature and density measurements of the Martian nightside ionosphere, *Geophys. Res. Lett.*, 42, 8854– 8861, doi:10.1002/2015GL065267.

Fowler, Christopher, New insights into the structure and energetics of the Martian ionosphere (2016). Astrophysical and Planetary Sciences Graduate Theses and Dissertations. 50. https://scholar.colorado.edu/astr_gradetds/50

Fowler, C. M., et al. (2018a), Correlations between enhanced electron temperatures and electric field wave power in the Martian ionosphere, *Geophys. Res. Lett.*, 45, 493–501, doi: 10.1002/2017GL073387.

Fowler, C. M., Andersson, L., Ergun, R. E., Harada, Y., Hara, T., Collinson, G., et al. (2018b). MAVEN observations of solar wind-driven magnetosonic waves heating the Martian dayside ionosphere. *Journal of Geophysical Research: Space Physics*, 123, 4129–4149. https://doi.org/10.1029/2018JA025208

Fox, J. L. (1993), The production and escape of nitrogen atoms on Mars, J. Geophys. Res., 98, 3297–3310, doi:10.1029/92JE02289.

Fox, J. L., and A. B. Hac (2009), Photochemical escape of oxygen from Mars: A comparison of the exobase approximation to a Monte Carlo method, Icarus, 204 (2), 527-544.

Gröller, H., Montmessin, F., Yelle, R. V., Lefèvre, F., Forget, F., Schneider, N. M., et al. (2018). MAVEN/IUVS stellar occultation measurements of Mars atmospheric structure and composition. Journal of Geophysical Research: Planets, 123, 1449–1483. https://doi.org/10.1029/2017JE005466

Jakosky, B.M., Lin, R.P., Grebowsky, J.M. et al. Space Sci Rev (2015) 195: 3. https://doi.org/10.1007/s11214-015-0139-x

Lillis, R. J., D. A. Brain, S. W. Bougher, F. Leblanc, J. G. Luhmann, B. M. Jakosky, R. Modolo, J. Fox, J. Deighan, X. Fang, et al. (2015), Characterizing atmospheric escape from Mars today and through time, with MAVEN, Space Science Reviews, 195 (1-4).

Lillis, R. J., et al. (2017), Photochemical escape of oxygen from Mars: First results from MAVEN in situ data, *J. Geophys. Res. Space Physics*, 122, 3815– 3836, doi:10.1002/2016JA023525.

Peterson, W. K., et al. (2016), Photoelectrons and solar ionizing radiation at Mars: Predictions versus MAVEN observations, J. Geophys. Res. Space Physics, 121, 8859–8870, doi:10.1002/2016JA022677

Peterson, W. K., Fowler, C. M., Andersson, L. A., Thiemann, E. M. B., Jain, S. K., Mayyasi, M., et al. (2018). Martian electron temperatures in the subsolar region: MAVEN observations

589 compared to a one-dimensional model. Journal of Geophysical Research: Space Physics,
590 123. https://doi.org/10.1029/2018JA025406.
591 Rees, M.H. (1989), Physics and chemistry of the upper atmosphere, Cambridge Atmospheric
592 and Space Science Series, Cambridge University Press, **ISBN:** 9780521368483
593 McFadden, J.P., et al. (2015), MAVEN SupraThermal and Thermal Ion Composition (STATIC)
594 Instrument, Space Sci. Rev., 195, 199, doi: 10.1007/s11214-015-0175-6.
595 Mahaffy, P., et al. (2015), The Neutral Gas and Ion Mass Spectrometer on the Mars Atmosphere
596 and Volatile Evolution Mission, Space Sci. Rev., 195, 49, doi:10.1007/s11214-014-0091-1.
597 Matta, Majd et al., (2014), Numerical simulations of ion and electron temperatures in the
598 ionosphere of Mars: Multiple ions and diurnal variations, Icarus, 227, 78,
599 doi:10.1016/j.icarus_2013.09/006.
600 Mendillo, M., Narvaez, C., Vogt, M. F., Mayyasi, M., Forbes, J., Galand, M., … Andersson,
601 L. (2017). Sources of ionospheric variability at Mars. *Journal of Geophysical Research: Space*
602 *Physics*, 122, 9670– 9684. https://doi.org/10.1002/2017JA024366
603 Mitchell, D.L. C. Mazell, J.-A. Sauvaud, J.-J. Thocaven, J. Rouzaud, A. Fedorov, P. Rouger,
604 D. Toublanc, E. Taylor, D. Gordon, M. Robinson, S. Heavner, P. Turin, M. Diaz-
605 Aguado, D. W. Curtis, R. P. Lin, and B. M. Jakosky (2016), The MAVEN solar wind electron
606 analyzer (SWEA), Space Sci. Rev. xx, 34, doi: 10.1007/s11214-015-0232-1.
607 Morrison, M. A., and A. E. Greene (1978), Electron cooling by excitation of carbon dioxide, J.
608 Geophys. Res., 83(A3), 1172–1174, doi:10.1029/JA083iA03p01172.
609 Nagy, A.F, J.P. Doering, W.K. Peterson, M.R. Torr, and P.M. Banks (1977), Comparison Between
610 Calculated and Measured Photoelectron Fluxes from Atmosphere Explorer C and E, J.
611 Geophys. Res. 82, 5099, doi: 10.1029/JA082i032p05099
612 Sakai, S., et al. (2016), Electron energetics in the Martian dayside ionosphere: Model
613 comparisons with MAVEN data, J. Geophys. Res. Space Physics, 121, 7049–7066,
614 doi:10.1002/2016JA022782.
615 Sakai, S., Cravens, T. E., Andersson, L., Fowler, C. M., Mitchell, D. L., Mazelle, C., et al. (2019).
616 Low electron temperatures observed at Mars by MAVEN on dayside crustal magnetic field
617 lines. Journal of Geophysical Research: Space Physics, 124. https://
618 doi.org/10.1029/2019JA026961
619 Schunk, Robert, and Andrew Nagy (2009), *Ionospheres: Physics, Plasma Physics, and Chemistry,*
620 Cambridge University Press.
621 Shinagawa, H., and T. E. Cravens (1989), A one-dimensional multi-species
622 magnetohydrodynamic model of the dayside ionosphere of Mars, J. Geophys. Res., 94,
623 6506, doi:10.1029/JA094iA06p06506.
624 Stone, S. W., Yelle, R. V., Benna, M., Elrod, M. K., & Mahaffy, P. R. (2018). Thermal structure of
625 the Martian upper atmosphere from MAVEN NGIMS. Journal of Geophysical Research:
626 Planets, 123, 2842–2867. https://doi.org/10.1029/2018JE005559
627 Thiemann, E. M. B., P. C. Chamberlin, F. G. Eparvier, B. Templeman, T. N. Woods, S. W.
628 Bougher, B. M. Jakosky (2017), The MAVEN EUVM model of solar spectral irradiance
629 variability at Mars: Algorithms and results, J. Geophys. Res. Space Physics, 122, 2748–2767,
630 doi:10.1002/2016JA023512.

631 Thiemann, E. M. B., Andersson, L., Lillis, R., Withers, P., Xu, S., Elrod, M., et al. (2018). The Mars
632 topside ionosphere response to the X8.2 solar flare of 10 September 2017. *Geophysical*
633 *Research Letters*, 45,8005– 8013. https://doi.org/10.1029/2018GL077730
634 Withers, P., K. Fallows, and M. Matta (2014), Predictions of electron temperatures in the Mars
635 ionosphere and their effects on electron densities, Geophys. Res. Lett., 41, 2681–2686,
636 doi:10.1002/2014GL059683.
637 Xu, S., Thiemann, E., Mitchell, D., Eparvier, F., Pawlowski, D., Benna, M., al.,
638 et (2018). Observations and modeling of the Mars low-altitude ionospheric response to
639 the 10 September 2017 X-Class solar flare. *Geophysical Research Letters*, 45, 7382–
640 7390. https://doi.org/10.1029/2018GL078524.

Figure 1.

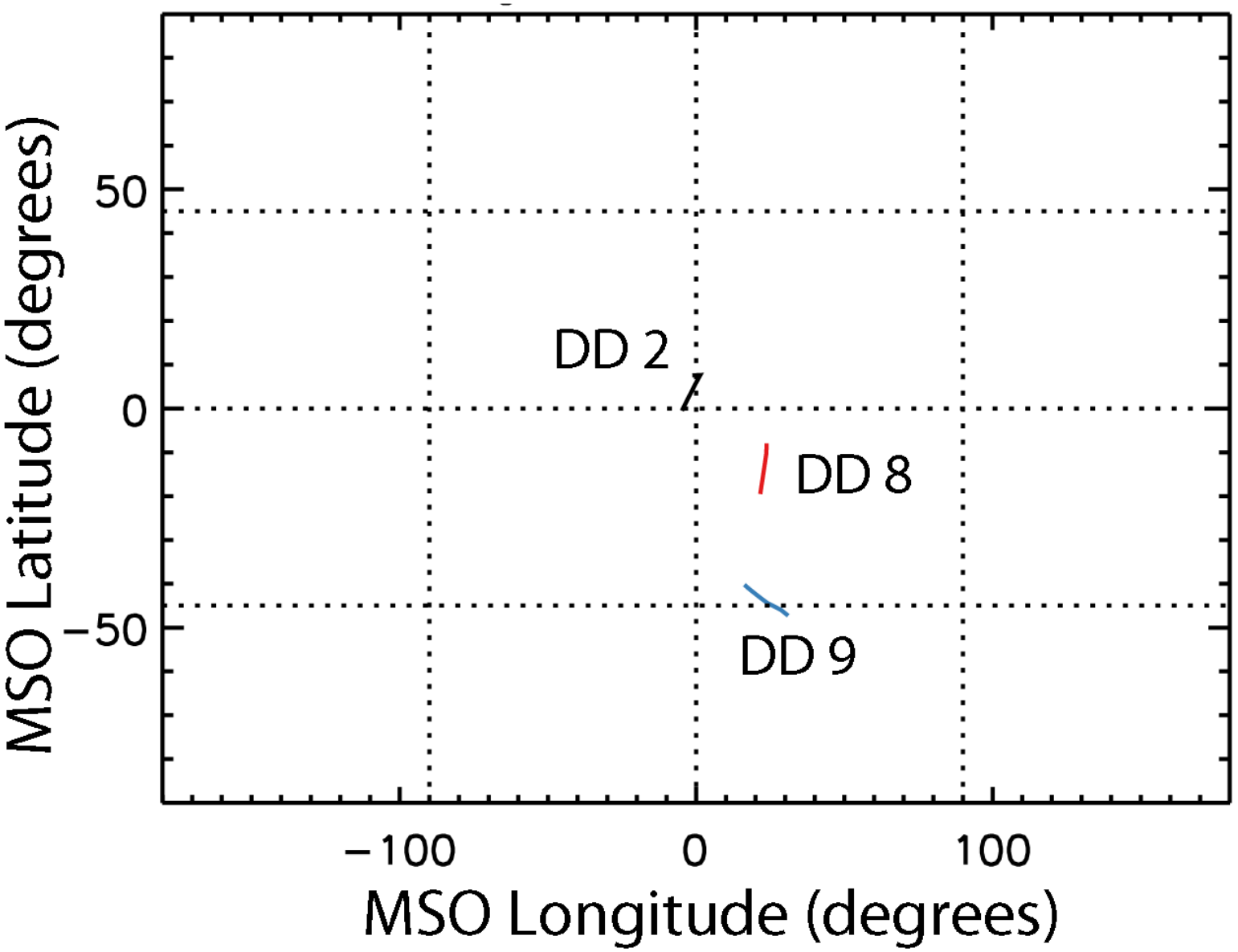
MSO Latitude (degrees)
50
0
−50
DD 2
DD 8
DD 9
−100
0
100
MSO Longitude (degrees)

Figure 2.

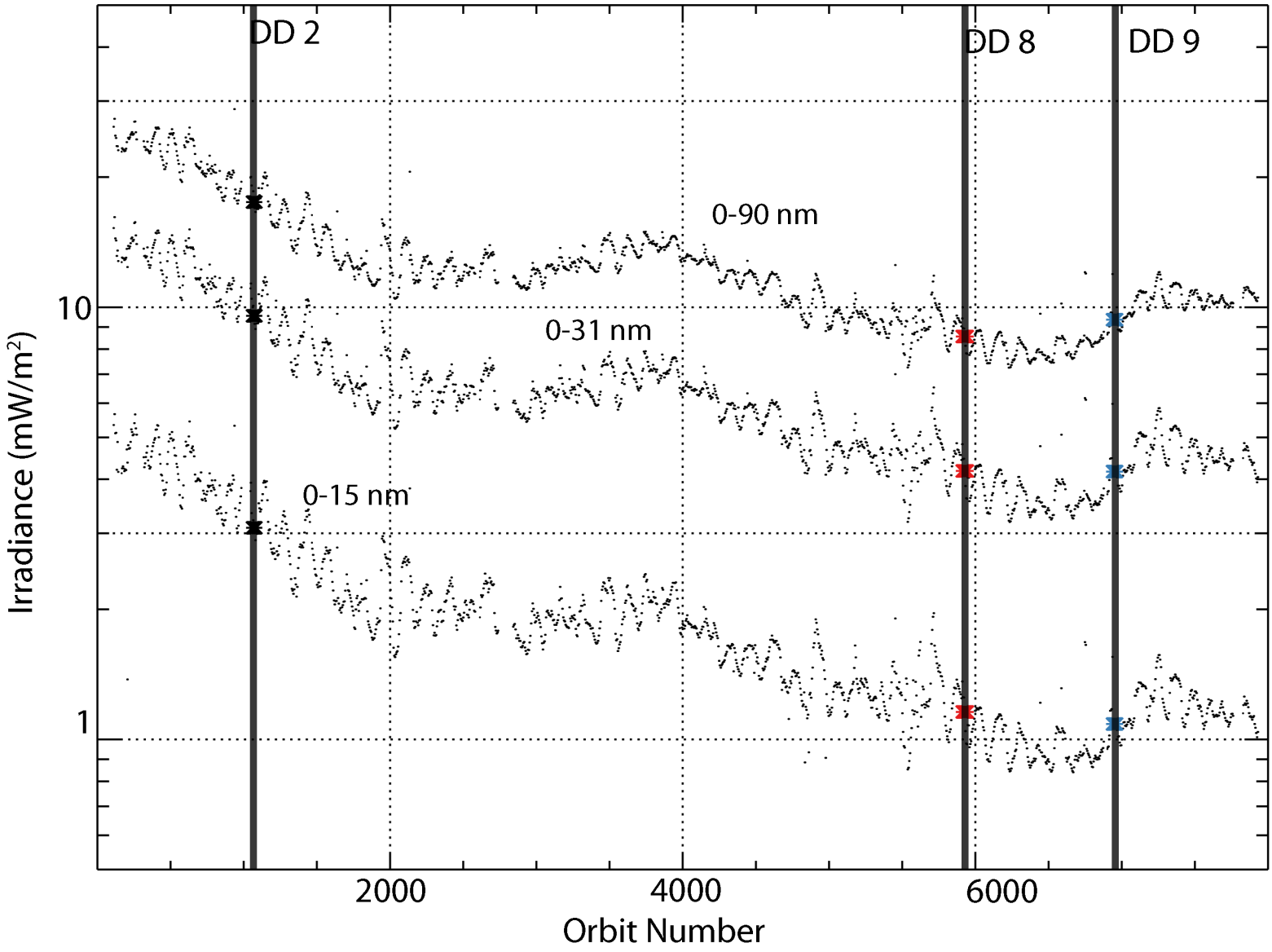
DD 2
DD 8
DD 9
0-90 nm
0-31 nm
0-15 nm
10
1
Irradiance (mW/m²)
2000
4000
6000
Orbit Number

Figure 3.

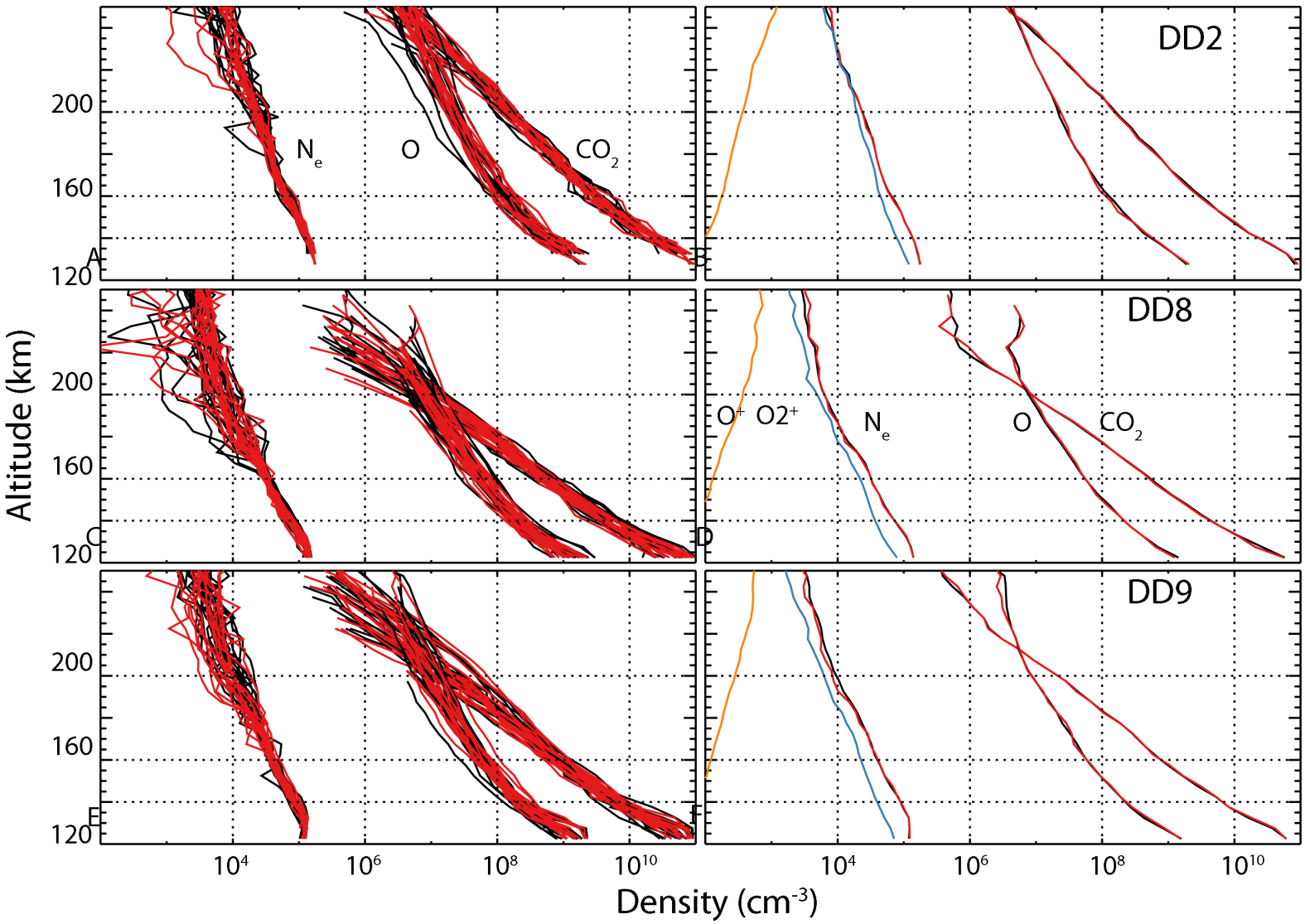
DD2
DD8
DD9
Altitude (km)
Density (cm-3)
Ne
O
CO2
O+
O2+
A
B
C
D
E
F
120
160
200
10^4
10^6
10^8
10^10

Figure 4.

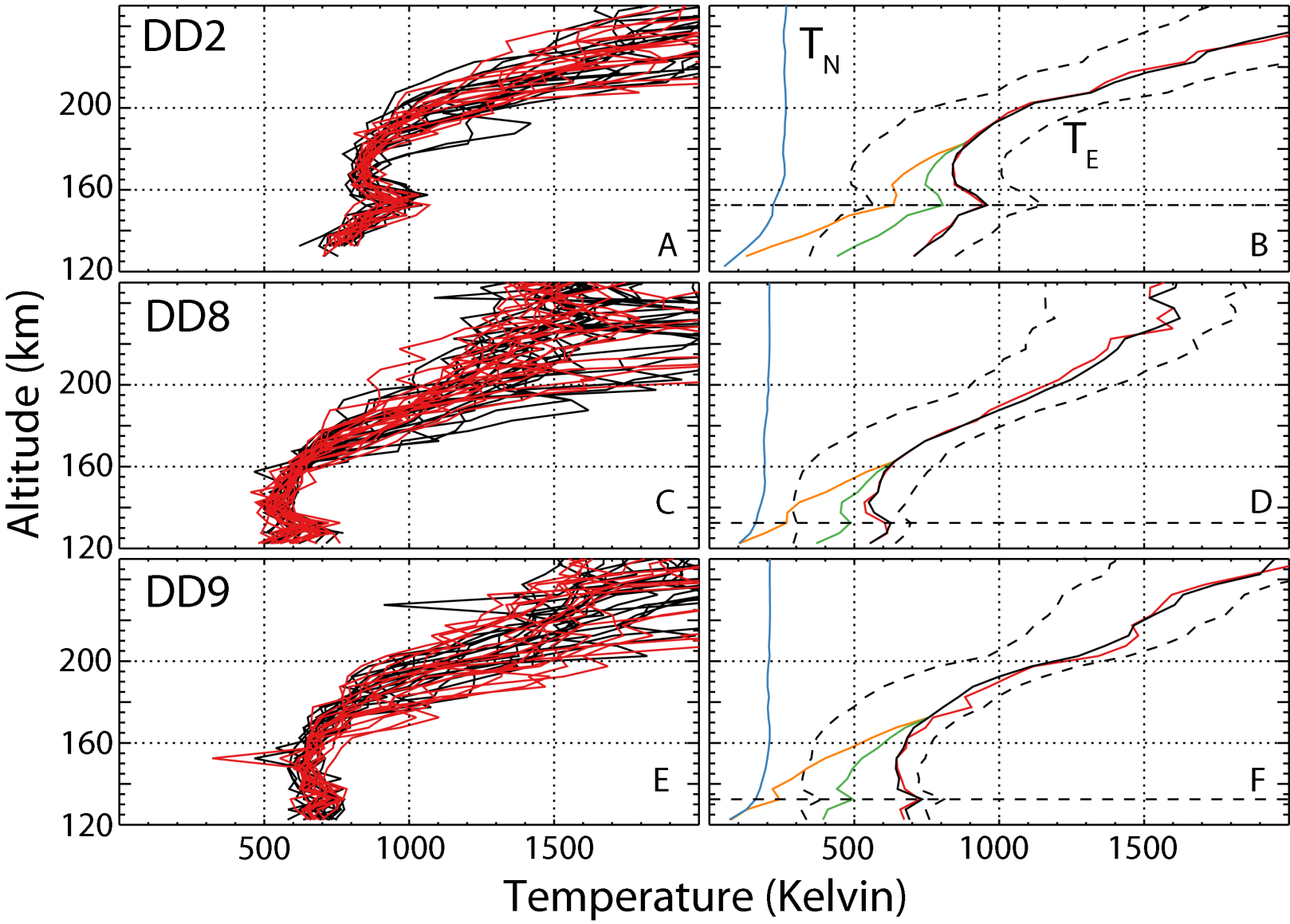
DD2
DD8
DD9
A
B
C
D
E
F
T_N
T_E
Altitude (km)
120
160
200
500
1000
1500
Temperature (Kelvin)

Figure 5.

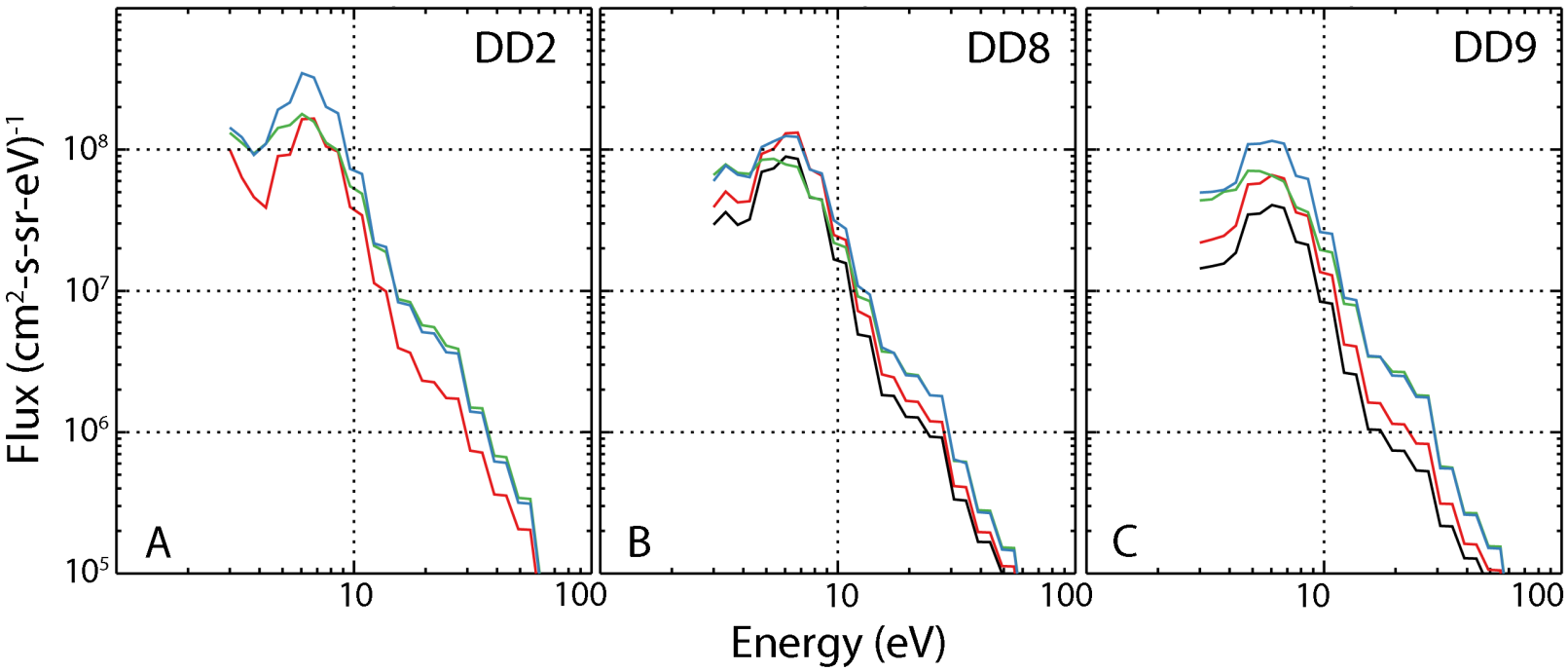
DD2
DD8
DD9
A
B
C
Flux (cm^2-s-sr-eV)$^{-1}$
10^8
10^7
10^6
10^5
10
100
Energy (eV)

Figure 6.

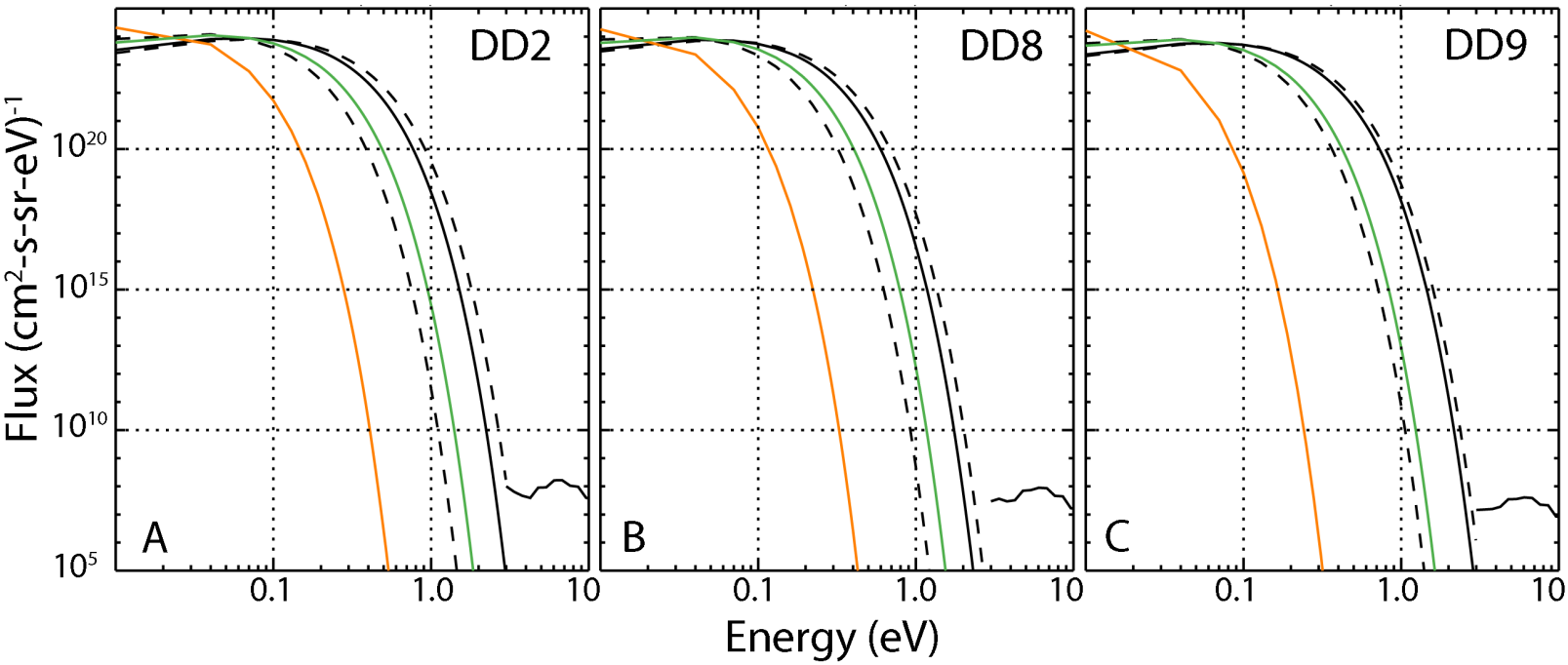
DD2
DD8
DD9
A
B
C
Flux (cm^2-s-sr-eV)$^{-1}$
10^{20}
10^{15}
10^{10}
10^{5}
0.1
1.0
10
Energy (eV)

Figure 7.

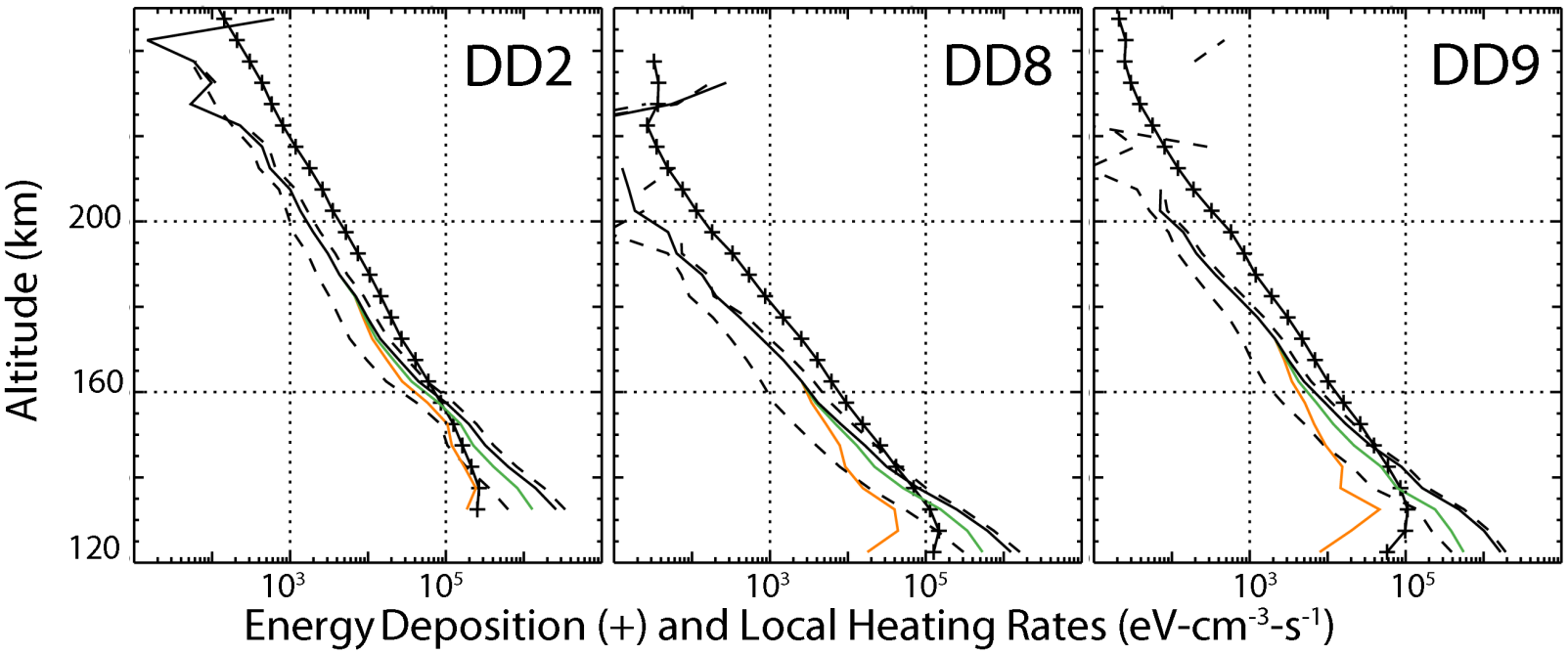
DD2
DD8
DD9
Altitude (km)
200
160
120
10^3
10^5
Energy Deposition (+) and Local Heating Rates (eV-cm^{-3}-s^{-1})

Figure 8.

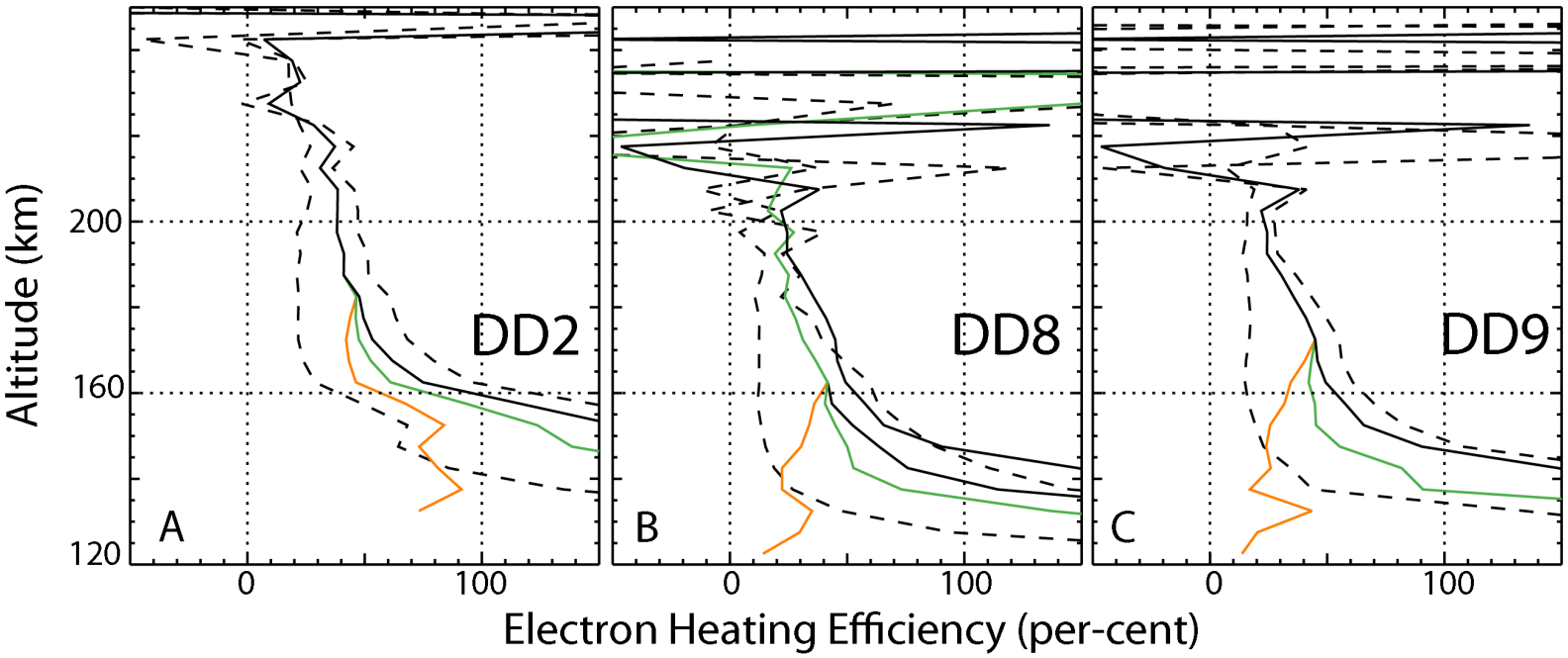
Altitude (km)
200
160
120
DD2
DD8
DD9
A
B
C
0
100
0
100
0
100
Electron Heating Efficiency (per-cent)

Figure 9.

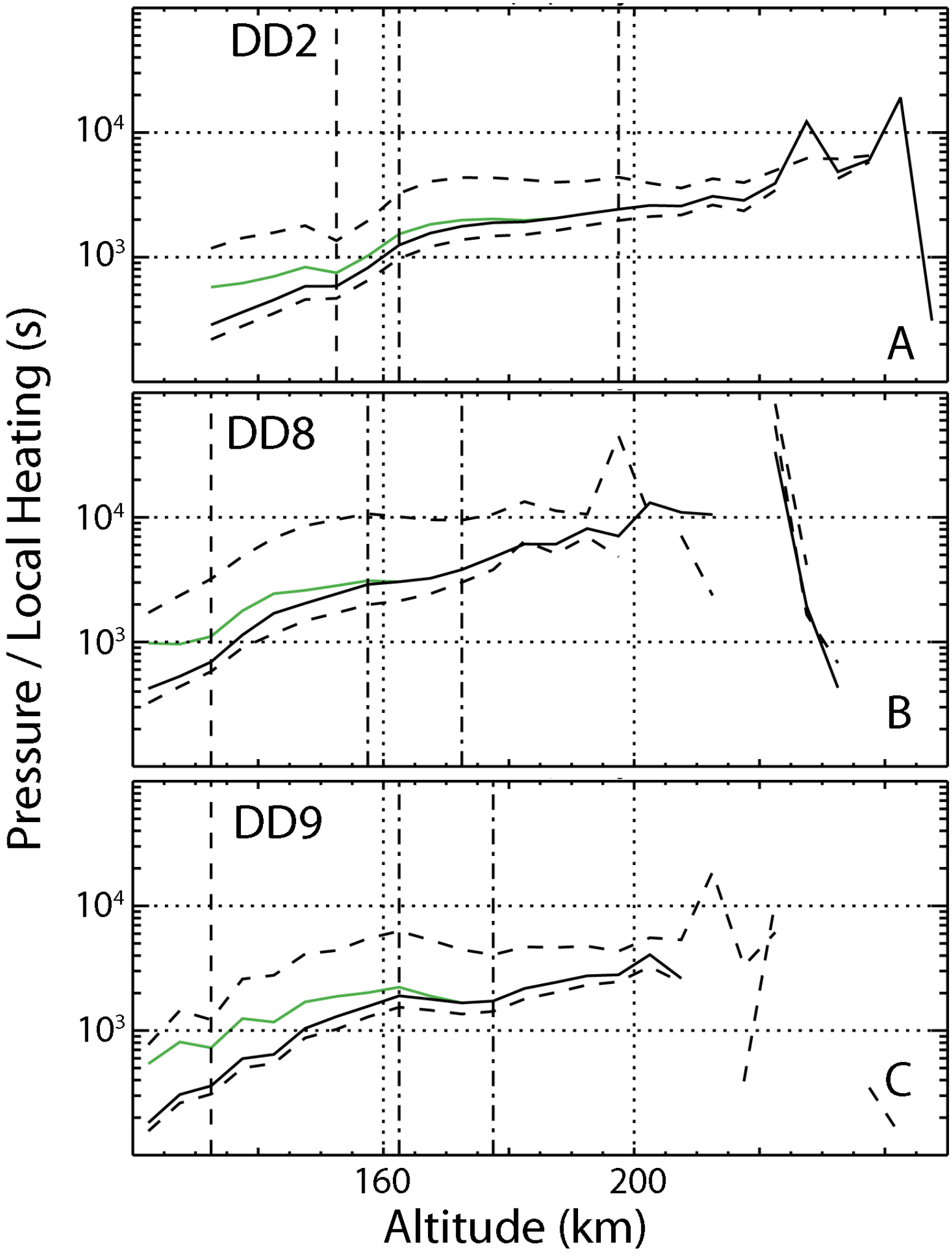
DD2
DD8
DD9
A
B
C
10^4
10^3
160
200
Pressure / Local Heating (s)
Altitude (km)

Figure 10.

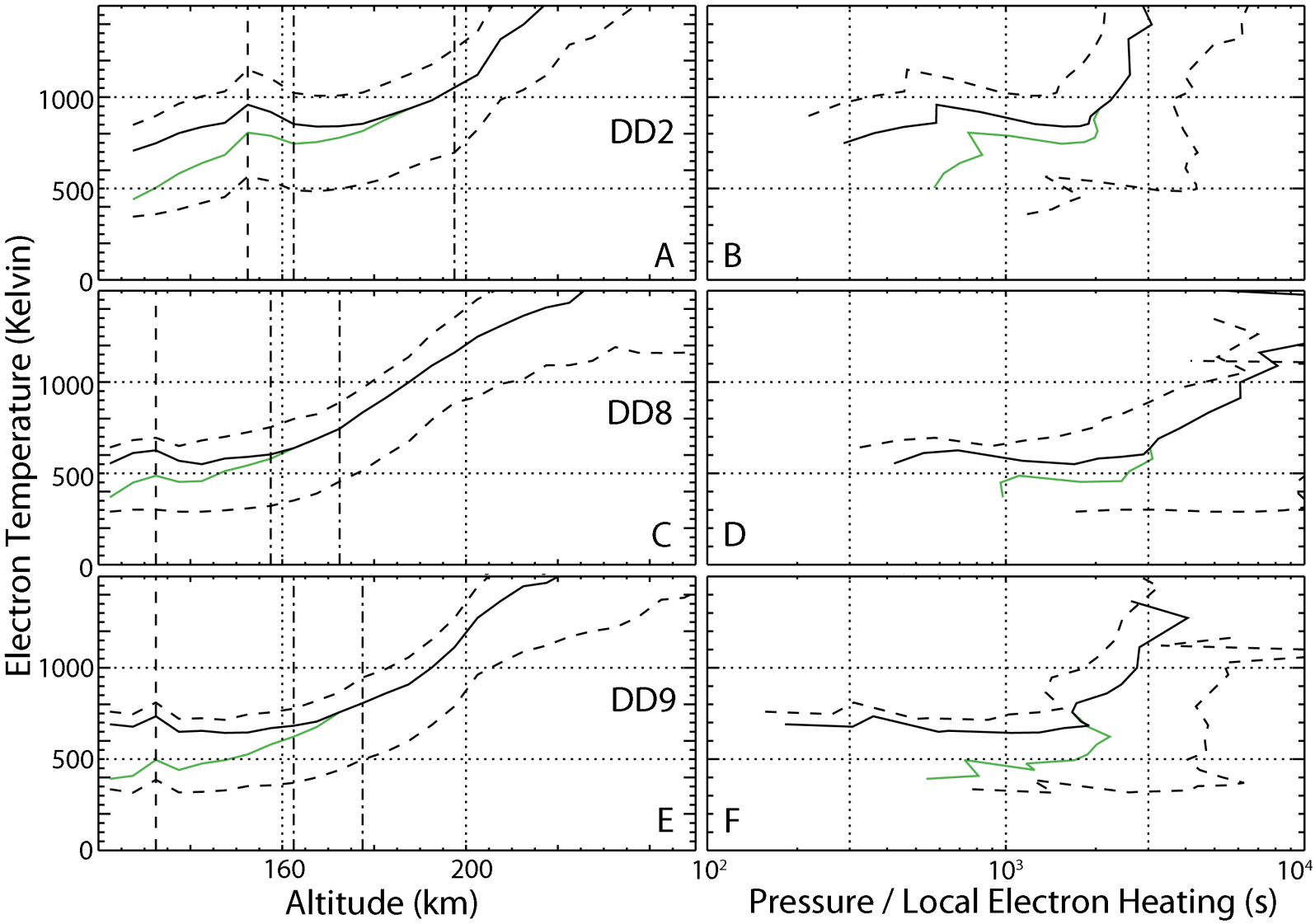
Electron Temperature (Kelvin)
0
500
1000
DD2
A
B
DD8
C
D
DD9
E
F
160
200
Altitude (km)
10^2
10^3
10^4
Pressure / Local Electron Heating (s)

Figure 11.

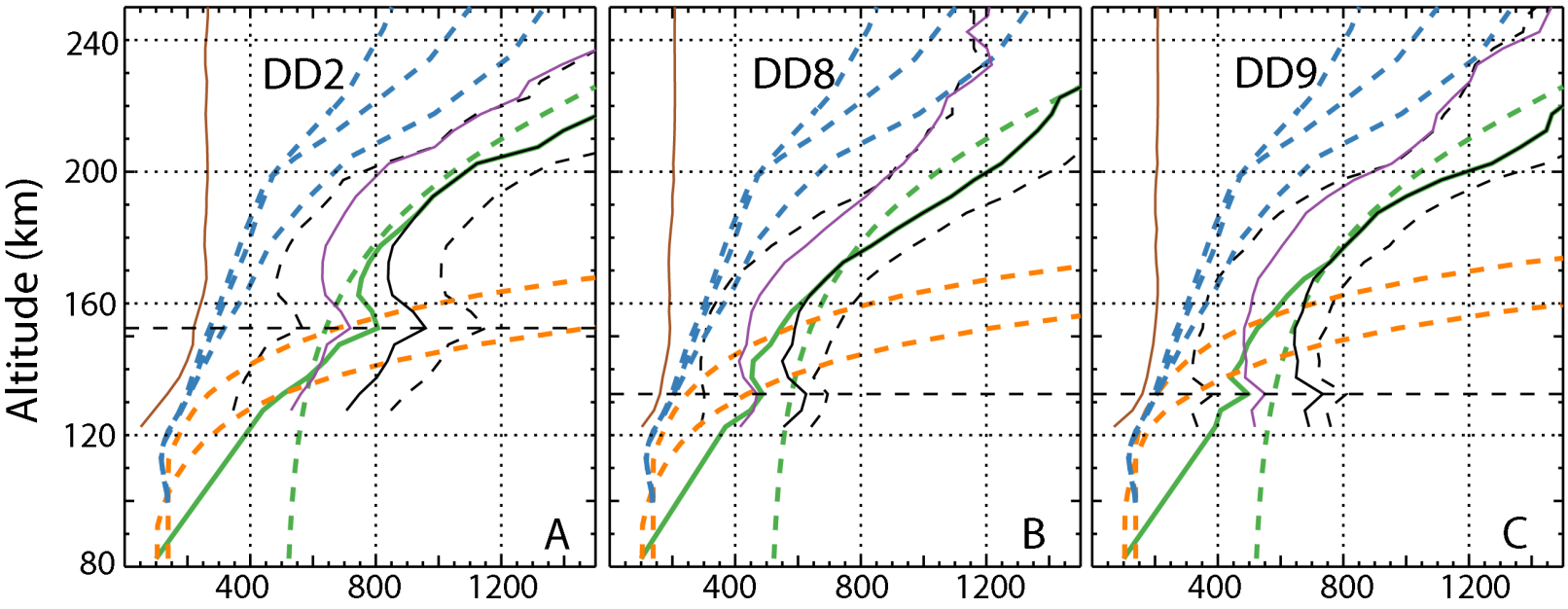
Altitude (km)
240
200
160
120
80
DD2
DD8
DD9
A
B
C
400
800
1200